



On the effects of reorientation and shear transfer during twin formation: Comparison between high resolution electron backscatter diffraction experiments and a crystal plasticity finite element model

Hamidreza Abdolvand*, Angus J. Wilkinson

Department of Materials, University of Oxford, Parks Road, Oxford, OX1 3PH, UK

ARTICLE INFO

Article history:

Received 25 January 2016

Received in revised form 11 April 2016

Available online 24 May 2016

Keywords:

A. Twinning

B. Crystal plasticity

B. Polycrystalline material

High resolution EBSD

ABSTRACT

The effects of reorientation and twin shear transfer on the load sharing between twin and parent pairs in hexagonal closed-pack (HCP) polycrystals have been examined by combined experimental and numerical methods. A highly textured Zircaloy-2 sample was uniaxially strained in a direction that favours twin formation and then unloaded to measure variations in residual elastic strains, lattice rotations, and stresses within twin and parent grains by the use of high resolution electron backscattered diffraction (HR-EBSD). The measured grain structures were imported into a finite element solver to study local stresses within each grain and their evolution as twins form. A crystal plasticity finite element code was modified to integrate the effect of twin shear strain into the constitutive equations. Results show that between reorientation and twin transformation strain, the later plays the more important role on determining the state of the stress in the parent, twin and the surrounding environment. The elastic energy of the parent grain was shown to reduce upon twin formation but then stay constant after the early stages of twin shear transfer. This can promote the formation of the next twin in preference to increasing the size of the current one. Comparison of the model with HR-EBSD measurements took into account that the residual stress variations were measured relative to the (unknown) stress state at the reference point within each grain.

© 2016 The Author(s). Published by Elsevier Ltd. This is an open access article under the CC BY license (<http://creativecommons.org/licenses/by/4.0/>).

1. Introduction

In the absence of easy slip systems, deformation by twinning plays a significant role in accommodating an externally applied strain. In low symmetric crystals, twinning can be dominant major deformation mechanism for deformation at high strain rates (Brown et al., 2012; Morrow et al., 2016), at low temperatures (Kauffmann et al., 2011), or even at room temperature (Gong et al., 2015). Unlike slip, twinning is a dynamic process that results in abrupt change of poly-crystalline texture. At fundamental levels, understanding various aspects of deformation twinning is important because twinning can have several significant effects on materials behaviour. For instance, it is shown that under uniaxial loading, twinning has significant contribution to the ductility of magnesium alloys (Agnew and Duygulu, 2005), however, formability or ductility

* Corresponding author.

E-mail addresses: hamidreza.abdolvand@materials.ox.ac.uk, hamid.abdolvand@gmail.com (H. Abdolvand).

under multiaxial deformation of those alloys at room temperature are much less than other light alloys, e.g. Aluminium. It is argued that the micro-textures that are induced by twinning are the probable reason for such low formability (Barnett, 2007; Timár and da Fonseca, 2014). Further, it is also known that stress concentration at the intersection of two twins can provide enough driving force for crack nucleation in low stacking fault energy face centered cubic (FCC) polycrystals (Müllner et al., 1994). We have recently shown that for an HCP polycrystal, twins intersections have highest geometrically necessary dislocation density (GND) concentration associated with them (Abdolvand and Wilkinson, 2016). Similarly, it is recently shown that twin intersection with grain boundary in nanocrystalline materials can be a potential site for nano-crack nucleation depending on the twin thickness and orientation relationship between twin plane and grain boundary geometry (Ovid'ko and Sheinerman, 2014).

Such observations provide enough motivation to study various aspects of deformation twinning. For instance, variant selection during twin formation in HCP polycrystals have been studied in detail as preference in selecting a particular variant could result in significant macroscopic shape change (Abdolvand and Daymond, 2013a; Beyerlein et al., 2010; Capolungo et al., 2009). It is shown that the most stressed twin variant is not always the variant that result in twin formation, yet in most of the cases it contributes the most (Abdolvand et al., 2015a). Selection of particular twin variant can be influenced by the tri-axial state of stress at the twin nucleation site. The effects of various parameters on twin nucleation were recently studied by Cheng and Ghosh (2015) with the use of a new non-local Crystal Plasticity Finite Element (CPFE) Model. An energy based criteria was used for twin nucleation where the initial energy of the system had to be greater than a critical value to have successful twin. This is compatible with what was suggested by Clausen et al. (2008) - the driving force for twin nucleation is higher than the one required for propagation. This leads to development of a back stresses that could influence the state of stress within twin itself (Barnett et al., 2013; Muránsky et al., 2009, 2013b; Wu et al., 2008). Further, twinning is a polarized process in which changing the loading direction can cause de-twinning to occur. Effects of twinning and de-twinning on the texture development in magnesium AZ31 alloy has been studied by Proust et al. (2009) using crystal plasticity in a self-consistent framework. Based on this model, effects of strain path changes on texture evolution of beryllium was studied by Knezevic et al. (2013a). In order to replicate effects of strain path changes, it was crucial to assign different rate of dislocation density evolution to each slip system. With the use of the same numerical framework coupled to experimental neutron diffraction and acoustic emission measurements, deformation mechanism of randomly textured magnesium has recently been studied where it was shown that both slip and twinning are the dominant deformation mechanism during uniaxial loading (Máthis et al., 2015). Load sharing between twin and parent pairs is an aspect of twinning that has been investigated in detail (Brown et al., 2005; Muránsky et al., 2013a; Wang et al., 2013). Neutron diffraction experiments on Mg alloys have shown that twins are relaxed compared to the parent grains (Brown et al., 2005; Clausen et al., 2008). These experiments provide an average stress over all those twins that can diffract the incident beam. Understanding stress variation within each twin and parent required a higher spatial resolution technique.

At smaller scale, micromechanics of deformation twinning has also been studied using various techniques. For instance, formation of twins in steel has been studied by the use of micro-compression pillars where it was shown that the critical resolved shear stress required for activating twinning and dislocation glide were essentially the same (Choi et al., 2015). Similarly, with the use of nano-indentation and CPFE simulation, it was shown that tensile twins form on the surface of indented magnesium sample, independent of the orientation of the grain that was indented (Zambaldi et al., 2015).

Analysis of twins is accessible through the use of high resolution electron backscatter diffraction (HR-EBSD) technique (Troost et al., 1993; Wilkinson, 1996). With this method, Kikuchi patterns collected at various positions within each crystals are cross-correlated using digital image correlation technique. This will provide shifts in the features of collected patterns that can be transformed into elastic strain and elastic lattice rotation. Relative deviatoric stress can be extracted directly by measuring pattern shifts; however, by adding an extra equation where surface normal stresses are set to zero, hydrostatic stress can also be extracted, so as a result the whole stress tensor can be accessed (Wilkinson et al., 2006). Initial work (Wilkinson et al., 2006) found that using image based cross-correlation, pattern shifts can be measured with sub-pixel precision with subsequent precision of 10^{-4} in elastic strain and 10^{-4} rad in lattice rotation measurements. More recent measurements have shown that with pattern averaging the precision can be improved further by at least a factor of two (Britton et al., 2013). The SEM provides great flexibility allowing HR-EBSD to map large areas for statistical analysis on the state of deformation, or small regions at high magnification targeting specific microstructural features. For instance, the technique has recently been used to study the evolution of dislocations in more than 1600 grains over $0.5 \times 0.5 \text{ mm}^2$ regions of various copper samples (Jiang et al., 2015). While much smaller maps ($\sim 10 \times 20 \text{ }\mu\text{m}$) at the intersections of slip bands and grain boundaries have been used to study very localised stresses and GND density distributions near dislocation pile-ups (Britton and Wilkinson, 2012a; Guo et al., 2014).

In this paper HR-EBSD technique will be used to study deformation twinning. One remaining issue with the HR-EBSD technique is that strains and lattice variations within a grain are measured relative to a user selected reference point within the grain. In many cases the strain state at the reference point is unknown so that the absolute strain values are not known (the so-called reference pattern problem). Karamched and Wilkinson (2011) were the first to use modelling to address the reference pattern problem by using continuum plasticity FEM simulations to calculate the average elastic strain values within a small region mapped using HR-EBSD in a Ni-based superalloy bend sample and then offsetting the HR-EBSD results to match this average value. More recently Zhang et al. (2014) used more localised CPFEM modelling of residual stress near oxide inclusions in a poly-crystalline Ni-based superalloy and subtracted strains at the reference to make quantitative comparison with HR-EBSD to validate the model.

In parallel to the experimental study of deformation twinning, crystal plasticity has played significant role in understanding fundamentals of the process. Major contributions to the field were given by Van Houtte (1978), Tomé et al. (1991), Kalidindi (1998), and Staroselsky and Anand (2003). In this framework, twinning comprises of two steps; in the first step, part of the parent grain must be reoriented to account for texture development as a result of twinning. The most active twin variant, also known as the predominant variant, was suggested to be used for determining twin orientation based on that of the corresponding parent (Tomé et al., 1991). In the second step, the shear caused by twinning is modelled as pseudo-slip with the magnitude of shear strain proportional to the magnitude of the resolved shear stress acting on the twin plane (Kalidindi, 1998). To model the evolution of twin size, the twin volume fraction was suggested to be proportional to this pseudo-shear (Kalidindi, 1998; Salem et al., 2005; Izadbakhsh et al., 2011). As twinning is often accompanied by a significant shear transfer, e.g. 0.169 and 0.129 for tensile twins in zirconium and magnesium, respectively, the problem with the pseudo-shear method is that the “true” effect of shear transfer during twin formation cannot be captured (Kumar et al., 2015).

In order to understand deformation partitioning between twin and parent, in this study, the effect of reorientation and shear transfer during twin formation is studied in detail. Residual elastic strains and lattice rotation variations within grains of a deformed Zircaloy-2 sample were measured using HR-EBSD technique. The measured grain map is then imported in to the ABAQUS finite element solver (Abaqus, 2014) to model twin formation by a crystal plasticity finite element model. Various assumptions for the state of twin during nucleation and propagation were examined within the CPFE code and the result of each compared against HR-EBSD measurements. Further, calculated average stress within twin and parent pairs during twin formation are compared against previously published data for the same material obtained using three-dimensional synchrotron X-ray diffraction (Abdolvand et al., 2015c).

2. Sample preparation and experimental set up

A sample made of Zircaloy-2 with HCP crystal was used. This material has been well characterized with in-situ neutron diffraction (Xu et al., 2008a), EBSD (Abdolvand and Daymond, 2013b), 3DXRD (Abdolvand et al., 2015b), and finite element modelling (Abdolvand et al., 2011). This sample was uniaxially strained up to 2.7% with strain rate of $\dot{\epsilon} = 5 \times 10^{-5} \text{ s}^{-1}$. Since the sample was highly textured, the load was applied in the direction that favours twin formation. An inverse pole figure-x map of the sample is shown in Fig. 1a where the loading direction coincide with the indicated x-axis. The sample was polished after unloading to provide a better quality Kikuchi patterns for HR-EBSD measurement. Mechanical polishing was performed using silicon carbide papers down to 4000 grit followed by polishing in 50 nm colloidal silica suspension for about 2 h. PECS-II ion polisher was used to prepare the final surface using 7.5 keV beam energy under dual beam condition, with gun angle of 8° and for about 15 min. This setting resulted in collecting excellent patterns even close to highly deformed area, e.g. twin tips.

All of the measurement was carried out in a MERLIN Field Emission Gun Scanning Electron Microscope (FEG-SEM) with 20 keV beam energy, 15 nA current, and working distance of 18 mm. A Bruker high resolution EBSD detector was used to collect 800×600 Kikuchi images with 180 milli seconds exposure time per collected pattern. This setting provides reasonable collection time for measuring an entire map while retaining precise measurement of relative elastic strains and lattice curvature for GND density estimation (Britton et al., 2013; Jiang et al., 2013a, c). For measuring residual elastic strains and lattice rotations, Kikuchi patterns collected within each grains were cross-correlated with the pattern acquired at a reference point that was chosen far away from stress concentration sites, i.e. HR-EBSD provides “relative” variations of elastic strains, stresses, and lattice rotations within each grain. In order to enhance the quality of cross-correlation, each Kikuchi pattern was firstly divided into 40 square regions which consist of 128×128 pixel images. After transforming each of these regions into the Fourier domain, high and low pass filters were applied to remove background intensity gradients and noise. By cross-correlating these regions it is possible to calculate pattern shifts. Assuming that stress normal to the surface is zero, relative elastic strain, lattice rotation, and stress tensors can be calculated fully (Wilkinson et al., 2006).

The presence of large ($>10^\circ$) lattice rotations that are often found after plastic deformation generate pattern shifts that are an order of magnitude greater than those from elastic strains which can lead to errors in the strain calculations. To overcome this, the remapping technique described in Britton and Wilkinson (2012b) was used to improve the results. With this method, a first pass of the cross-correlation analysis establishes a lattice rotation which is used to inform a remapping of the pattern intensity, using bi-cubic interpolation, so as to effect a virtual rotation of the test pattern into the reference pattern orientation. A second pass of the cross-correlation analysis comparing the rotated test patterns and the original reference pattern is then used to determine the elastic strain tensor and any remaining correction to the lattice rotation. The deformation gradients from the first and the second passes are finally combined to determine the total deformation gradient from which the Green strain tensor is calculated.

3. Crystal plasticity modelling

3.1. Constitutive equations

A user material subroutine (UMAT) for modelling large elastic–plastic deformation induced by slip and twinning was developed by Abdolvand and Daymond (2013b). This approach is modified and used in the current work for simulating local deformation during twin formation. As described in Section 1, deformation by twinning has been historically modelled as pseudo-slip which is suitable for calculating average stress or texture development of aggregates (Ardeljan et al., 2015; Chang

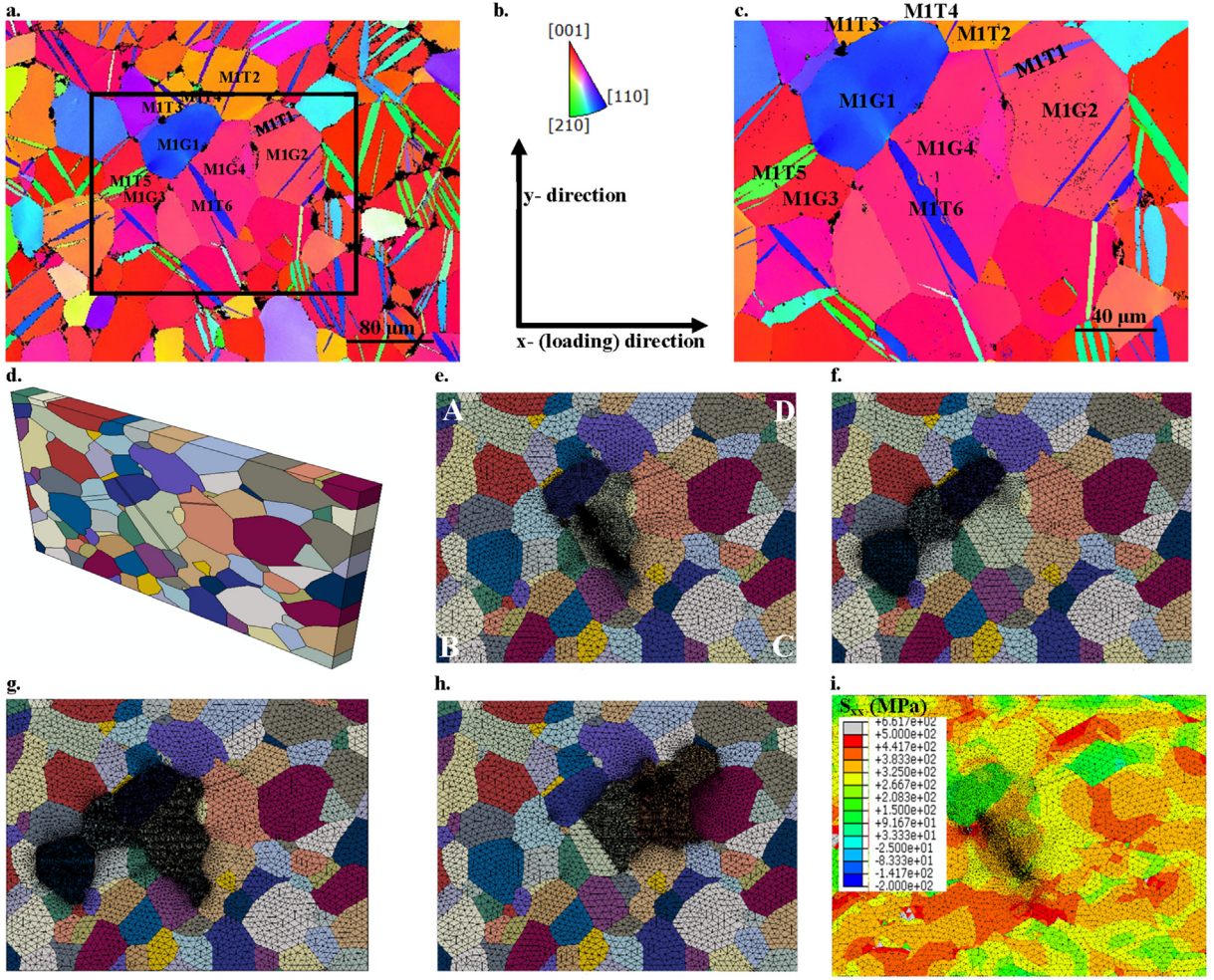


Fig. 1. (a) An inverse pole figure-x of the sample with the coordinate system and colour codes shown in (b). (c) An HR-EBSD scan of the centre of the map presented in (a). (d) Grain structure of map (a) imported into ABAQUS CAE for simulation. Meshed models used for simulating (e) M1T6, (f) M1T5, (g) M1T5 and M1T6 together, (h) M1T1. (i) An example of calculated stress in the loading direction with M1T6 model for macroscopic applied strain $\epsilon_{xx} = 0.33\%$.

and Kochmann, 2015; Knezevic et al., 2013b). It has recently been suggested that if the actual stress field close to individual twin boundary is the subject of interest, it is crucial to model the shear transfer during twin formation (Kumar et al., 2015; Knezevic et al., 2016). Therefore, we have modified our UMAT to incorporate the effect of the twin transformation strain. In the UMAT, at each time step, total strain, total rotation, and time increment are given by the ABAQUS FE solver (Abaqus, 2014), and the task is to calculate stress increment, update solution dependent state variables (SDVs), and to update the Jacobian matrix ($J = \frac{\partial \Delta \sigma}{\partial \Delta \epsilon}$). Following the framework proposed by Kumar et al. (2015), we calculate the elastic and plastic strain increment as:

$$\Delta \epsilon = \Delta \epsilon^{el} + \Delta \epsilon^{pl} + \Delta \epsilon^{tr} \quad (1)$$

where $\Delta \epsilon$ is the total strain increment given by the FE solver, $\Delta \epsilon^{el}$ is the elastic strain increment, $\Delta \epsilon^{pl}$ is the plastic strain increment as a result of slip, and $\Delta \epsilon^{tr}$ is the transformation strain as a result of twinning. First we write the components of the strain tensor in the rate form and then integrate them to calculate the increments. The rate of the plastic strain ($\dot{\epsilon}^{pl}$) or plastic part of deformation rate (\dot{D}^{pl}) can be calculated using the following equation:

$$\dot{\epsilon}^{pl} = \dot{D}^{pl} = \sum_{\alpha=1}^{N^{spl}} P^{\alpha} \dot{\gamma}^{\alpha} \quad (2)$$

$$P^{\alpha} = \text{sym}(S^{\alpha}) \text{ where } S^{\alpha} = d^{\alpha} \otimes n^{\alpha}$$

in which P^α is the symmetric part of the Schmid tensor (S^α) for the slip system α , $\dot{\gamma}^\alpha$ is the shear rate on slip system α . d^α and n^α are the slip direction and normal of the system α , respectively. A rate dependent equation is used for calculating the slip shear rates (Asaro and Needleman, 1985):

$$\dot{\gamma}^\alpha = \dot{\gamma}_0 \left| \frac{\tau^\alpha}{g^\alpha} \right|^n \text{sign} \left(\frac{\tau^\alpha}{g^\alpha} \right) \quad (3)$$

where $\dot{\gamma}_0$ is a reference shear strain rate and n controls the rate dependency. τ^α and g^α are the resolved shear stress on the slip system α and strength of this system, respectively. The strength of each slip system (g^α) is assumed to follow an extended Voce hardening (Tome et al., 1984):

$$g^\alpha = g_0^\alpha + (g_1^\alpha + \theta_1^\alpha \Gamma) \left(1 - \exp \left(- \frac{\theta_0^\alpha \Gamma}{g_1^\alpha} \right) \right) \quad (4)$$

where g^α is the current critical resolved shear stress (CRSS), g_0^α is the initial CRSS, Γ is accumulated shear on all slip systems, θ_0^α is initial hardening rate, and g_1^α and θ_1^α determine asymptotic characteristics of hardening.

The resolved shear stress (in Eq. (3)) is proportional to the Kirchhoff stress (Ψ) through the following equation (Asaro, 1983):

$$\tau^\alpha = P^\alpha : \Psi \quad (5)$$

The Jaumann rate of Kirchhoff stress ($\dot{\tilde{\Psi}}$) is related to the elastic part of the rate of deformation (\dot{D}^{el}) and the elastic stiffness tensor (\mathbb{C}) as:

$$\dot{\tilde{\Psi}} = \mathbb{C} : \dot{D}^{el} \text{ where } \dot{\tilde{\Psi}} = \dot{\Psi} - \dot{\Omega}^{el} \Psi + \Psi \dot{\Omega}^{el} \quad (6)$$

where $\dot{\Omega}^{el}$ is the elastic part of the rotation tensor. The deformation and the rotation rates are correlated to the symmetric and asymmetric parts of the velocity gradient (L) as:

$$(\dot{D}^{el} + \dot{D}^{pl}) + (\dot{\Omega}^{el} + \dot{\Omega}^{pl}) = \text{sym}(L) + \text{asym}(L) \quad (7)$$

and the plastic part of the rotation increment is correlated to the plastic shear rate and asymmetric part of the Schmid tensor (W^α):

$$\dot{\Omega}^{pl} = \sum_{\alpha=1}^{N^{spl}} W^\alpha \dot{\gamma}^\alpha \quad (8)$$

The twinning transformation strain is applied incrementally during the transformation phase (see Section 3.2) until the characteristic twin shear for zirconium (0.169) is fully applied into the *twinned domain*:

$$\begin{aligned} \Delta \gamma^{tw} &= \frac{0.169}{T_{TST}} \Delta t \\ \Delta \epsilon^{tr} &= S^{tw} \Delta \gamma^{tw} \end{aligned} \quad (9)$$

where T_{TST} is the total time used for applying twin transformation strain and is assumed to be 3060 s, Δt is the time increment defined by FE solver during each increment of transformation phase, and S^{tw} is the twin variant Schmid factor.

3.2. Input model and boundary conditions

Several twins were modelled to study the influence of various assumptions on the stress development within twin and parent pairs during nucleation and propagation stages. For this purpose, the three twins, M1T1, M1T6, and M1T5, located in the middle of the EBSD map shown in Fig. 1b were modelled and studied in detail. These twins were selected as they provide interaction of twin with both a soft neighbouring grain, i.e. M1G1, and a hard neighbouring grain, i.e. M1G4. There are no easy slip systems providing plastic elongation or contraction along the crystal c-axis. Thus grains such as M1G4 oriented with the crystal c-axis close to the tensile axis are hard, while grains that have their crystal c-axis close to normal to the loading direction, e.g. M1G1, are soft (See Fig. 1a and i). In order to avoid the effects of boundary conditions on the calculated stresses a bigger EBSD map was measured where the studied twins and neighbouring grains were at least three grains away from the map edges. This EBSD map is presented in Fig. 1a and it covers an area of $409 \times 307 \mu\text{m}^2$ of the sample surface. A series of codes were developed to determine grain boundaries and import them as an image into the ABAQUS CAE. Previous studies carried out on the same material has shown that the sample is almost twin free before any load is applied (Abdolvand and

Daymond, 2013b); therefore, all of the twins were removed from the microstructure imported into the FE solver. Since a twin can generate shear strain out of the x-y plane (see Fig. 1b), the imported microstructures were given a thickness in the third dimension so that the required deformation in the z-direction can be accommodated. A thickness of 25 μm was used which is equal to the measured average grain radius of the sample. The imported microstructure is shown in Fig. 1d.

It is important to recognise the compromise between 2D and 3D aspects of the model that are made in meshing the microstructure. The crystallography is captured in full 3D, however the grain morphology relies on the 2D EBSD mapping and so assumptions need to be made for the depth axis. Lacking any other knowledge we follow the most often used approach of simply projecting the 2D structure along the depth direction to form columnar grains (Lim et al., 2014; Zhang et al., 2014, 2015; Zhao et al., 2008). The effects of 3D microstructure below the 2D surface of observation can be large as has been elegantly shown in the crystal plasticity simulation of Zeghadi et al (Zeghadi et al., 2007a, 2007b). The strains induced by twin formation are very localized and we believe that this localization makes these features less affected by the arrangement of sub-surface grains (though certainly not unaffected). The 3D nature of the twin shear and its subsequent effects on the induced localized deformation are studied here and are presented in Appendix C.

The orientation of each grain for CPFE calculation are those that are measured using EBSD, however, the intra-granular orientation variations at the beginning of loading phase were neglected, i.e., the average measured orientation of each grain was used for modelling. Since crystals in Zircaloy-2 undergo only minor orientation change at small applied strains (Abdolvand et al., 2011), the measured, grain averaged, orientation at the end of deformation were imported to the CPFE model. It is worth mentioning that orientation variation within each grain that results from elastic and plastic deformation is allowed in the CPFE calculation once the load is applied (see Eqs. (6)–(8)). Previous *in-situ* neutron diffraction coupled with self-consistent modelling carried out on the material has indicated that the deformation of Zircaloy-2 is mostly controlled by prism $\langle 11\bar{2}0 \rangle$, basal $\langle 11\bar{2}0 \rangle$, and pyramidal $\langle 11\bar{2}3 \rangle$ slip as well as tensile twinning $\langle 10\bar{1}1 \rangle$ (Xu et al., 2008b, 2009). The material properties that are used for modelling in this paper are given in Table 1, and are those that are reported in Abdolvand and Daymond (2013b) for coarse grain size Zircaloy-2. The elastic properties of the single crystal is assumed to be identical to those of pure zirconium determined by Fisher and Renken (1964): $C_{11} = 143.5$ GPa, $C_{33} = 164.9$ GPa, $C_{12} = 72.5$ GPa, $C_{13} = 65.4$ GPa, and $C_{44} = 32.1$ GPa.

Depending on which twin was modelled, various mesh densities were assigned to the model presented in Fig. 1d where more elements were used in the areas that the modelled twins were nucleated and propagated. In order to have a better representation of the shapes of the grain boundaries and to avoid numerical instabilities that can be caused by the shape of the elements, C3D6 wedge elements were used for meshing the models. This is a continuum linear element that has two integration points (IP) and 6 nodes (Abaqus, 2014).

The boundary conditions used in modelling was $u_x = 0$ on the AB face shown in Fig. 1e, $u_y = 0$ on the BC face, and $u_z = 0$ on the AD face. These three boundary conditions were maintained during all of the modelling phases. Modelling deformation of the microstructure was carried out through six different phases. During the first phase the model was cooled down from 650 °C to the room temperature to include the effects of residual stresses that can develop during annealing of the sample. During the loading phase, a uniaxial strain was applied to the model up to 2.7% with the strain rate of $\dot{\epsilon} = 5 \times 10^{-5} \text{ s}^{-1}$. The uniaxial strain was applied through a constant velocity on the CD face shown in Fig. 1e. The total strain ϵ_{11} shown in Fig. 2a for the end of the loading phase appears a little lower than the 2.7% applied in the experiment but this is accounted for by the thermal contraction occurring during the cooling phase of the simulation. In the third phase, called reorientation here, the part of the parent grain that is twinned was reoriented to the measured twin orientation. This reorientation was applied only to the elements of the parent grain that fall into the observed twin domain. As stress state of the twinned domain is altered as a result of both reorientation and the assumptions that were tested (see below), and to avoid numerical instabilities caused by the swift reorientation of the twin domain, this phase was assumed to happen over a 1 s interval with initial time increment of 10^{-5} and maximum time increment of 0.3 s; with this step setting, the reorientation phase was normally accomplished within 30 increments. At phase four, called twin shear transfer (TST), the 0.169 twin shear was applied to the twin domain inside the UMAT under a constant macroscopic applied strain, i.e., the velocity applied to the CD face was set to zero during the reorientation and shear transfer phases. It was assumed that the TST happens over 3060 s which produces a strain rate of $\dot{\epsilon} = 5 \times 10^{-5} \text{ s}^{-1}$. With this assumption, the TST took place over 620 increments that provide a stable simulation at the expense of losing the dynamic effects of twin formation. In the phase five, the constant velocity applied to the CD face was removed to unload the sample and in phase six the sample was allowed to relax and reach the steady state condition. A schematic of the average strain in the loading direction and the twin shear transfer as a function of increments are shown in Fig. 2a.

The input model set up used for studying formation of various twins are given in Table 2. It has been shown that 350 IPs per grain will result in reasonable estimation of inter- and intra-granular stress heterogeneities (Diard et al., 2005; Musienko

Table 1
Single crystal properties of Zircaloy-2 (Abdolvand and Daymond, 2013b).

	n	$\dot{\gamma}_0 \text{ s}^{-1}$	g_0^α GPa	g_1^α GPa	θ_0^α GPa	θ_1^α GPa
Prism	20	3.5×10^{-4}	0.111	0.33	0.009	0
Basal	20	3.5×10^{-4}	0.156	0.22	0.044	0
Pyramidal	20	1.0×10^{-4}	0.307	0.27	0.551	0.28

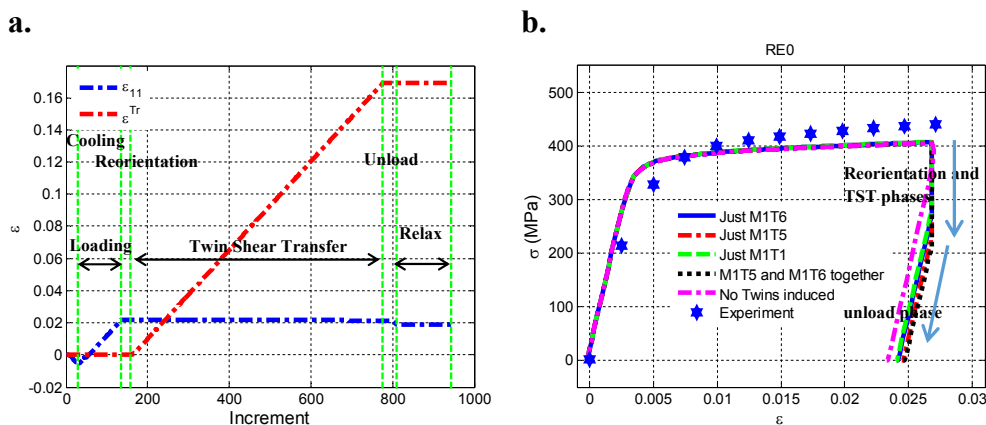


Fig. 2. (a) The average strain in the loading direction and the twin transformation strain applied to the twinned domain as a function of the increments used in CPFE modelling. (b) Comparison between calculated average stress–strain curves in the loading direction for different models with the measured one. Loading direction coincides with the x-axis shown in Fig. 1b.

Table 2

Number of elements used for each Abaqus input model.

	Modelling twin M1T1	Modelling twin M1T6	Modelling twin M1T5	Modelling twin M1T5 and M1T6
Total number of elements	107,112	70,864	84,448	166,088
Number of elements assigned to the twin and associated neighbouring grains	72,960	44,360	52,232	128,480
Corresponding figure	Fig. 1h	Fig. 1e	Fig. 1f	Fig. 1g
Model name	M1T1	M1T6	M1T5	M1T5&T6

et al., 2007); in all of the models used here, on average, more than 2000 IPs were assigned to each grain. Since we will focus on the stress close to twins, more than 74,000 IPs were assigned to the parent grains that are studied here to reinforce the convergence of the results as well as the stability of numerical simulations. Results of a convergence study are documented in Appendix A.

Different assumptions were tested to determine their possible effects on the stress development of twin and parent pairs. It has been argued that twins are relaxed at the early stage of their formation (Brown et al., 2005; Clausen et al., 2008). In order to investigate such observation, the following assumptions were tested at the beginning of the reorientation phase and for each of the models mentioned above:

- The twin domain reoriented and the stress state of the twin domain at the very first increment of reorientation phase was set to zero; this simulation is called RE0.
- The twin domain reoriented but the stress state of the twin domain was not changed, i.e. stress within the twin at the first increment of reorientation phase was equal to that calculated in the last increment of loading phase; this simulation is called RENO.
- The twin domain was not reoriented but the stress state of the twin domain at the first increment of reorientation phase was set to zero; this simulation is called NRE0.
- The twin domain was not reoriented and the stress state of the twin domain was not changed; this simulation is called NRENO.

To summarize the last two sections, at the beginning of each time increment and for each IP, the FE solver sends strain, time, and rotation increments to the UMAT. The plastic strain increment over all of the IPs through all of the phases are calculated using Eqs. (2) and (3). However, during the TST phase and just for the IPs that fall into the twinned zone, Eq. (9) is also used to calculate the twin transformation strain resulting from twinning. Once the plastic strain and twin shear strain increments are calculated, the elastic strain increment can be calculated using Eq. (1) and hence the stress increment (Eq. (6)). At the first increment of the reorientation phase, in models RE0 and RENO, the measured orientation are assigned to the twin domain whereas in NRE0 and NRENO models, twin domain orientation is not changed. Also, two scenarios are tested where at the first increment of reorientation phase, stress within twin domain is set to zero (RE0) or kept equal to what it was before reorientation (RENO). Setting stress within twin zone helps stability of FE simulation since with reorienting slip systems in the twin domain, the initial calculated resolved shear stress will be less than the current strength of the system, however for the RENO and NRENO cases, the initial calculated resolved shear stress within the twin domain for the new orientation can potentially exceed the current strength of the system and hence destabilize simulations (see Eq. (3)). To avoid such numerical

instability, deformation by slip is deactivated for RENO and NRENO models. This assumption can be valid for small twins due to Hall-Petch effects, however it is not as twins thicken.

4. Results

The coordinate system that is used to represent results in this paper is the one that is shown in Figs. 1b and 3a where the x_1 or x -axis represents the loading direction, x_2 or y axis represents the transverse direction lying on the sample surface, and x_3 or z points to the thickness of the sample and it is the right hand cross product of the other two axis. The “twin coordinate system” or the *local coordinate system* is defined where the *local*- x'_1 axis coincides with the twin shear direction, the *local*- x'_3 axis coincides with the normal to the twin habit plane and the *local*- x'_2 is the cross product of the other two. All of the results are given in the global coordinate system except for those that are titled with “in local coordinate” system.

4.1. HR-EBSD results

An inverse pole figure- x map of the investigated grains is shown in Fig. 3a. Since x represent the loading direction the red grains have their crystal c -axis oriented toward the loading direction. Thus it is expected that many of the red grains will twin which is seen to be the case. This map consist of a grid of 512×384 points that were measured with electron beam step-size of 441 nm with sample to detector and working distances of ~ 18 mm. Grains are labelled with an “M1” that represent the Map, and G or T that represent Grain or Twin followed by a unique number. In Fig. 3b to k the result of HR-EBSD calculations are shown. In Fig. 3b, a map representing the quality of the collected Kikuchi patterns is shown where most of the patterns have quality higher than 8 which is desirable for cross-correlating images. This quality is determined by the number of bands that are recognized by the EBSD software during indexing of crystal orientation and is influenced by surface polish quality and state of deformation at the interrogation point, amongst other things. The crosses indicated in Fig. 3b represent the reference points that are used to calculate the variations in elastic strains, lattice rotations, and stresses, i.e. these values for each grain are calculated with respect to the indicated reference point located within the grain. Since HR-EBSD provide the relative values, CPFE simulations are used to assist interpretation of the measured values (see Section 4.2).

In Fig. 3c to e the measure relative in-plane stresses are shown with the colour bars given in GPa. Generally, there is a high stress concentration associated with the grain and twin boundaries. For instance, in grain M1G1, there is a smooth transition from the reference point to the boundary shared with M1T6 and M1T5 where compressive stresses are measured in both normal directions. Since shear stresses are smaller than normal stresses, the colour bar in Fig. 3e is adjusted to acquire a better colour contrast. Similarly, there is a clear colour change happening within M1G1 close to M1T6 and M1T5 indicating stress concentration induced by twins located in the neighbouring grains (M1G4 and M1G3). A clear stress variation is observed in M1T6 where σ_{12} is positive in south tip while it is negative in north. On the other hand, all of the other stress components measured for M1T1 are relatively uniform probably as a result of good strain accommodation in neighbouring grains, and the relatively small twin size at the point when external loading was stopped.

Since zirconium has anisotropic elastic constants and to avoid the confusion resulted from the coupling terms in the elastic stiffness tensor, the measured relative elastic strains are also shown in Fig. 3f to h. General trends are similar to those explained for stress; for instance, similar to the measured relative stresses, elastic strains within M1G1 change smoothly toward the twin boundaries and turn into compression in the x_1 and x_2 directions. Since with HR-EBSD the elastic part of the deformation gradient can be calculated, it is possible to calculate the relative elastic lattice rotation within each grain. These measured rotations are illustrated in Fig. 3i to k. In these figures, Ω_{12}^{el} , Ω_{13}^{el} , and Ω_{23}^{el} represent elastic lattice rotation about the x_3 , x_2 , and x_1 axis where positive values reflect counter clockwise rotation. Similar to the stress and strain fields, there are higher concentrations close to the grain boundaries; interestingly, in the grain M1G1 a big change in the measured rotation field is captured close to shared boundaries with M1T6 and M1T5. These rotations are quite small about x_1 axis (Ω_{23}^{el} or out-of-plane rotations), but they are more significant about x_3 and x_2 axis. To understand the underlying reason for such trends CPFE simulations were performed and these trends are discussed in detail in the next section.

4.2. CPFE and HR-EBSD direct comparison

The $\{10\bar{1}2\}\langle\bar{1}011\rangle$ tensile twin system in zirconium has six variants for which we use the notation: variant-1, variant-2, variant-3, variant-4, variant-5, variant-6 to represent $(10\bar{1}2)[\bar{1}011]$, $(01\bar{1}2)[0\bar{1}11]$, $(\bar{1}102)[1\bar{1}01]$, $(\bar{1}012)[10\bar{1}1]$, $(0\bar{1}12)[01\bar{1}1]$, $(1\bar{1}02)[\bar{1}101]$, respectively. In the Appendix B, the measured orientation of each grain presented in Fig. 3a is given. Analysis of misorientation between normals to the basal planes within M1T6 and M1G4 indicated that variant-2 and variant-1 were the two candidates that could form M1T6 since their associated misorientation were $<7^\circ$. With matching the normal to the twin plane with the one from the morphology of the twin it was found that variant-2 was the most probable variant between the two. This was confirmed with simulating the twin orientation using parent measured orientation and a reflection tensor that was constructed by the normal to the twin habit plane. The same analysis was performed for the M1T5/M1G3 pair as well as for the M1T1/M1G2 pair where for both cases variant-5 was determined to be the active twin variant. The projections of twin shear on the x - y plane for M1T6/M1G4 and M1T5/M1G3 are shown in Fig. 3a. The projection of twin plane normal and twin shear direction are then used to construct the twin shear tensor (Eq. (9)) and apply it to the twin domain during the TST phase. There are two points that are required to be mentioned

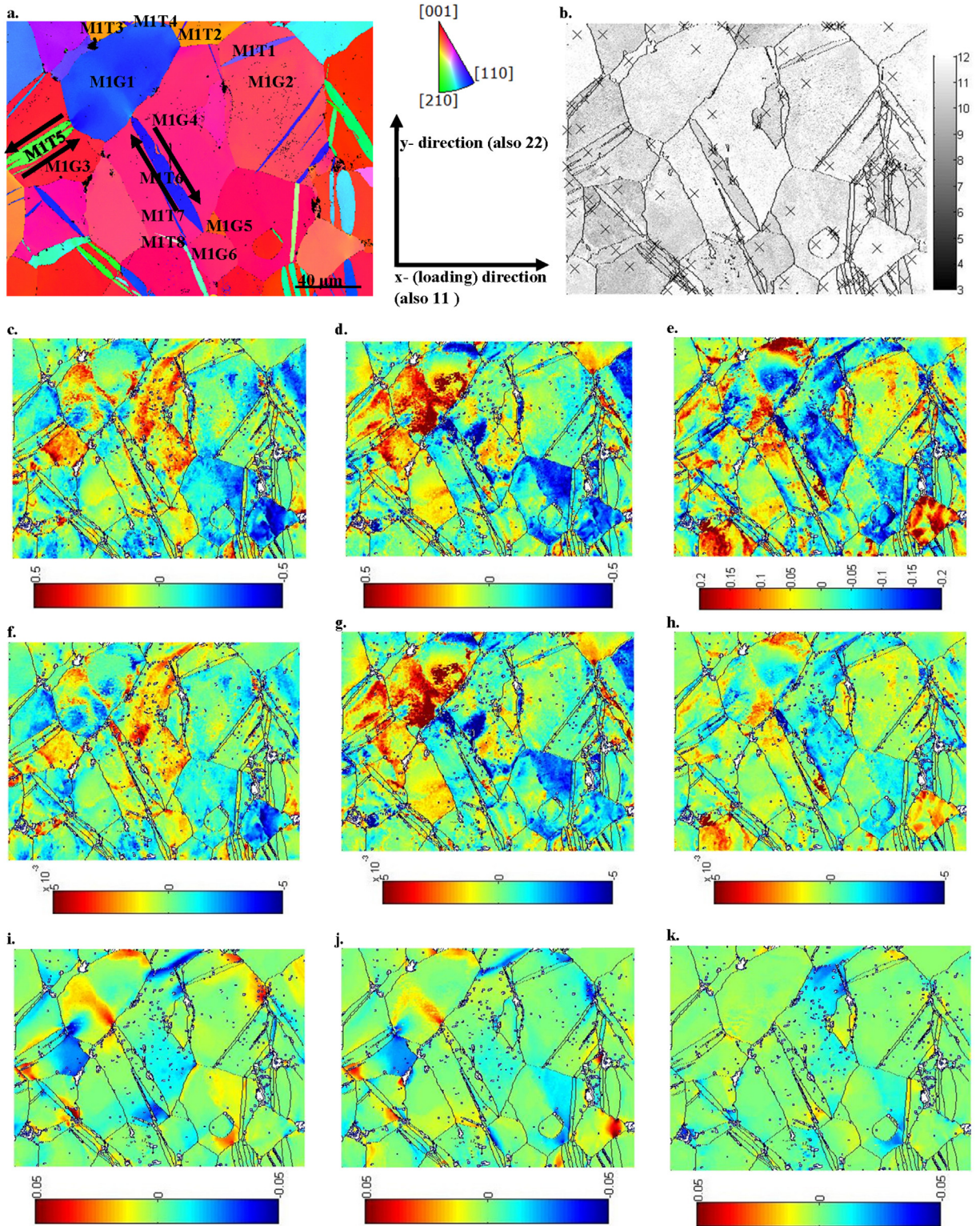


Fig. 3. (a) High resolution EBSD map of the investigated twins and parents with IDs assigned to each grain and twin. (b) Pattern quality map with crosses indicating the reference points used for the calculation of relative stresses or strains. (c) σ_{11} , (d) σ_{22} , and (e) σ_{12} are the relative stress maps; (f) ϵ_{11}^{el} , (g) ϵ_{22}^{el} , (h) and ϵ_{12}^{el} are the relative elastic strain maps; (i) Ω_{12}^{el} , (j) Ω_{13}^{el} , (k) and Ω_{23}^{el} are the relative elastic lattice rotation maps. Scale bar for each series is indicated under the figure where stresses, and rotations are given in GPa, and radians, respectively.

here. Firstly, although the 16.9% twin shear has out-of-plane components, applying it all within x-y plane provide an insight to the upper bound effects of such shear transfer. Appendix C compares results under this assumption with those in which the twin shear includes an out of x-y plane component. The lower bound is the case where no twin exists which is also studied numerically in what follows. Secondly, the effects of out-of-plane components of twin shear may not be modelled effectively in the current study as information regarding the under surface grains are missing in a given EBSD map. Such effects may be studied by the use of micro-Laue diffraction technique (Balogh et al., 2013). Further, modelling twin shear as a plane stress problem helps having stable simulation with minimum number of elements per model thickness, as accommodation of such shear requires a denser mesh to be assigned to the model thickness.

The average calculated stress–strain curves and the experimentally measured one are shown in Fig. 2b. The experimental stress–strain curve was acquired through the tensile experiment and it contains contributions from all of the grains in the sample, while for the calculated curve only the sub-set of grains imported to the Abaqus FE solver (Fig. 1a) contribute. In all of the models presented in Fig. 2b, after a cool down, uniaxial strain was applied up to 2.7% and then under constant strain, the twin domain is reoriented and plastically sheared to 16.9% after which the model was unloaded. The title “RE0” means that twin stress at the first increment of the reorientation phase was set to zero. To make a consistent comparison, all of the results of this section are with “RE0” assumption. The model “No Twin” represents the case where no twin was simulated and the model was simply unloaded after 2.7% straining. It is clear even from the average stress–strain curve that under constant strain, the average stress of the modelled grains drops during TST phase which follows with less residual elastic strain maintained within the system. The model indicates that this relaxation is a function of the twin size; for instance, the relaxation calculated for M1T1, with minimum twin size of the three cases studied here, is less than that calculated for M1T6 or M1T5&T6. In terms of comparison with the measured values, the average calculated stress–strain curves are slightly softer than the measured one; the single crystal parameters used in this study are those that are fitted with >2000 grains for the same material. It was shown that for the textured material that is used here, at least 500 grains must be modelled for replicating right stress–stress curve (Abdolvand et al., 2015c). In this study, only 93 grains are modelled which may not be representing the actual behaviour of the whole aggregate. More grains are needed for modelling to compensate the observed soft results.

4.2.1. Neighbour grain analysis

As an example of the effects of twin formation on the stress field within the neighbouring grain, stress evolution for M1G1 at different loading phases and for different modelling assumptions are shown in Fig. 4. Elastic strains, elastic lattice rotations, and in-plane stresses for different simulations are presented. In Fig. 4a and b, the states of M1G1 at the end of loading and TST phases for model M1T5&T6 are illustrated, respectively. In Fig. 4b, the shared boundaries with M1T5 and M1T6 are indicated with red circles where a big difference is observed in all of the illustrated components. For instance, stress and elastic strain in the loading direction (x_1) are particularly relaxed close to twin boundary after twin formation. Both M1T5 and M1T6 intensify the compressive transverse stresses σ_{22} existed at their shared boundaries with M1G1. The elastic shear strain and stress are rather different comparing to the normal component. For instance, at the intersection of the left edge of M1T6 with M1G1 a small region of intense positive shear is induced within M1G1 whereas a larger region of negative shear is induced at the right edge to provide a counter balance force for the positive local stresses. This is in agreement with the recent study on the effects of twin-type partial dislocations on the stress field in the neighbouring grains (Ovid'ko and Sheinerman, 2014). Similarly, M1T5 produces a negative and a positive shear field at the shared boundary with M1G1, however over a much bigger area since M1T5 is a thicker twin. In terms of rotation field, beside Ω_{23}^{el} where in all cases it is small and close to zero, different fields are induced in M1G1 close to the shared boundaries with the twins. For instance, formation of M1T6 increased the magnitude of Ω_{12}^{el} in the positive direction within M1G1. This counter balances the plastic rotation resulting from the twin plastic shear applied during TST phase. Since there is no applied rotation at the model boundaries, any rotation applied should be counter balanced to result zero average rotation. The twin plastic shear induced during formation of M1T6 is accompanied by a negative plastic rotation which is then counter balanced by a positive elastic rotation in the neighbouring grain M1G1. A similar trend is observed for M1T5, where the positive twin shear induces negative lattice rotations Ω_{12}^{el} and Ω_{13}^{el} within M1G1.

In order to compare the CPFE results and experimental HR-EBSD ones the state of M1G1 at the end of unload phase for the various modelling assumption and the HR-EBSD measurements are shown in Fig. 4c to h. The direct comparison between HR-EBSD and CPFE results are given in Fig. 4g and h where the reference point values for the model M1T5&T6 subtracted from every point in the simulation to mimic the reference pattern effect on the experimental data. In Fig. 4c, the CPFE results for the case where no twin was simulated is shown. In comparison to Fig. 4a, most of the tensile elastic strain and stress in the x_1 direction are replaced with a small compression in the left side of the grain. On the other hand, in the x_2 direction, a distinct tensile elastic strain are observed. In Fig. 4d, the results of the model including the M1T6 twin are illustrated in which not much change is observed in the ϵ_{11}^{el} and ϵ_{22}^{el} fields induced compared to the case where no M1T6 twin was included (Fig. 4c). However, a rather distinct difference is observed in both elastic lattice rotation fields and shear components.

In Fig. 4e, the result of the model M1T5 is presented to study the effect of M1T5 formation on variation of the stress field within M1G1. In contrast to M1T6, most of the components are altered including ϵ_{11}^{el} and ϵ_{22}^{el} . For instance, at the shared boundary with M1G1, a big compressive elastic strain and stress are observed in the x_1 direction at the unload phase which was not present if M1T5 was not modelled (Fig. 4c). The induced local rotation field is also significant. For the last case-study,

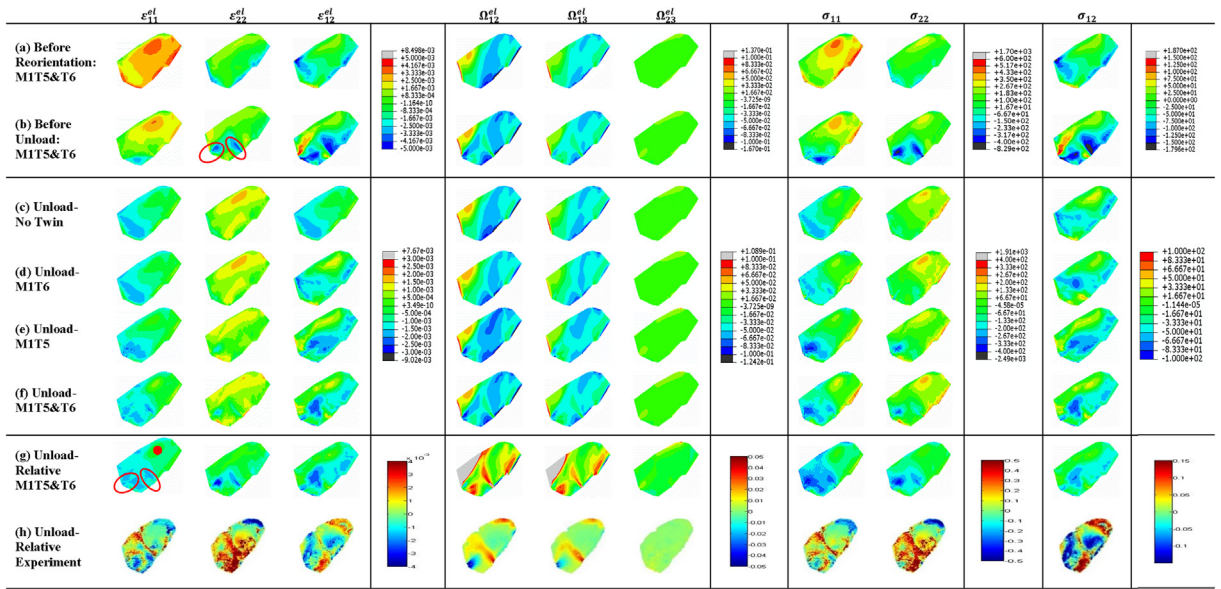


Fig. 4. Comparison between different model and assumptions for the grain M1G1: each model label is given in the first column, elastic strains are given in the second to the fourth column with the corresponding colour bar given in fifth column. Elastic lattice rotations are given in the sixth to the eighth columns with the corresponding colour bar in the ninth columns. Lattice rotations are given in radian. Normal stresses are given in the tenth and eleventh column with the corresponding colour bar given in the twelfth column. Shear strain and the related colour bar are given in the last two columns. Stresses are given in MPa and 11 coincides with the loading direction and 22 is the transverse direction (see Fig. 1b). The results of HR-EBSD are given in the last column (h) whereas the CPFE results with reference point reduced are presented in the rest. The reference point is shown with a red dot on CPFE ϵ_{11}^{el} and the boundaries that are shared with twins are indicated with circles. (For interpretation of the references to colour in this figure legend, the reader is referred to the web version of this article.)

the effect of superimposing formation of twins MIT5 and MIT6 are illustrated in Fig. 4f. For this case, a compressive elastic strain and stress field is observed in the x_1 direction close to the share boundaries with MIT5 and MIT6 where the later was not obvious when MIT6 was modelled alone (Fig. 4d). This reflects the coupling effects that MIT5 and MIT6 impose on each other. While ϵ_{22}^{el} and σ_{22} in Fig. 4f are not that different comparing to the case where MIT5 was the only modelled twin (Fig. 4e), the shear component ϵ_{12}^{el} and σ_{12} shows rather different trend particularly close to shared boundary with MIT6. This is also true for Ω_{12}^{el} and Ω_{13}^{el} lattice rotations. The extent of negative Ω_{12}^{el} rotation induced by MIT5 within M1G1 is much bigger than the case when this twin was modelled alone.

The effects of bringing the reference point values to zero by subtracting a uniform stress, elastic strain, and lattice rotation from the simulated fields (Fig. 4f) is shown in Fig. 4g. The relative results (Fig. 4g) appear very different compared to the actual ones (Fig. 4f). For instance, the positive Ω_{12}^{el} rotation field close to MIT6 is much more vivid in Fig. 4g while the region of negative Ω_{12}^{el} close to MIT5 is almost gone. This is also true for Ω_{13}^{el} . In both x_1 and x_2 directions elastic strains and stresses are compressive with higher values close to the twin tips. The calculated relative stresses are given in the same colour scale as the HR-EBSD results. A qualitative comparison between CPFE and HR-EBSD results shows that elastic strain and stress in the loading direction are in relatively close agreement with HR-EBSD results especially when attention is directed to the local areas close to the twin tips. The agreement is perhaps strongest for the relative elastic lattice rotation components. However the agreement is poorer for the elastic strain and stress in the transverse direction.

To shed more light on to this, a quantitative comparison between CPFE and HR-EBSD results for relative elastic strains and relative lattice rotations along lines directly ahead of the twin tips are given in Fig. 5. The CPFE results in these targeted locations are in outstandingly good agreement with HR-EBSD results for calculation of rotation fields. For instance, it is shown in Fig. 5a that both Ω_{12}^{el} and Ω_{13}^{el} increase toward the head of MIT6 where the magnitude of the rotation increases by at least two fold over a 20 microns distance. Meanwhile, both CPFE and HR-EBSD show almost no relative rotation about x_1 axis. These variations close to MIT5 tip within M1G1 is shown in Fig. 5c. At 25 microns distance from the MIT5 tip, both Ω_{12}^{el} and Ω_{13}^{el} are small and close to zero, however, both CPFE and HR-EBSD indicate a U-shape variation in these two components close to the twin tip. Similar to the MIT6 case, Ω_{23}^{el} is quiet small and close to zero over the entire investigated area. The better agreement between CPFE and HR-EBSD results for lattice rotation field is a result of using a large rotation formulation in the body of our CPFE calculation (see Eqs. (6)–(8)). Further, elastic lattice rotations are more than 20 times bigger than the elastic strains, that is why it is much easier to measure and track their variations with HR-EBSD (compare scales in Fig. 5a and c with Fig. 5b and d). These large rotations can potentially overshadow the movement of patterns and consequently the measurement of lattice strains. That is why we used a two-step calculation, also known as remapping technique, to acquire a better estimation of residual elastic strains with HR-EBSD technique. These elastic strains for M1G1 close to the head of MIT6 and MIT5 are shown in Fig. 5b and d, respectively. While in the loading direction ϵ_{11} reasonable agreement is achieved the results are quite different in the transverse direction ϵ_{22} . It is shown that deviation from crystal plasticity results as well as uncertainty in

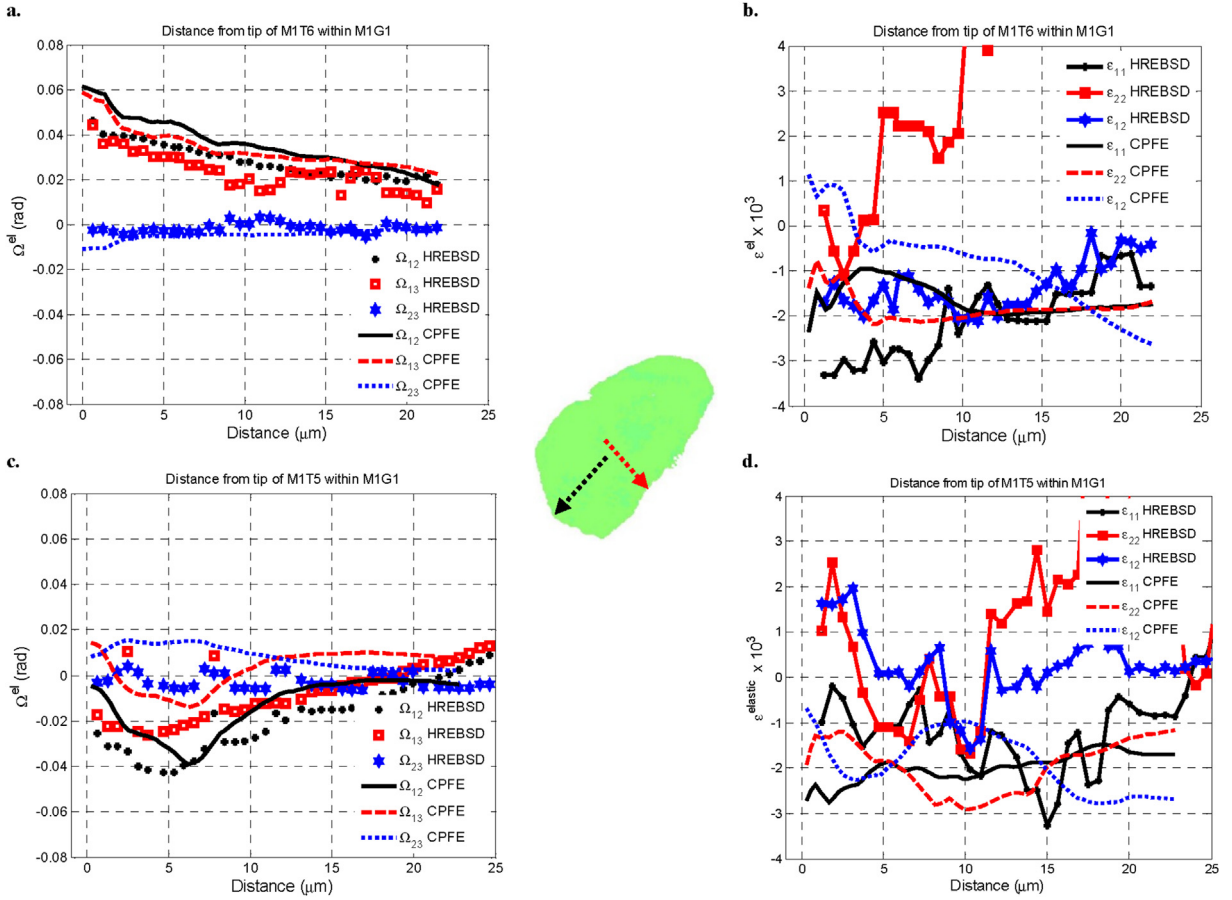


Fig. 5. Comparison between CPFE and HR-EBSD results for variation of (a and c) relative elastic lattice rotations and (b and d) relative elastic strains close to twin boundaries within the grain M1G1. For Fig. 5a and b results along the red arrow shown in the middle are presented whereas for Fig. 5c and d those along the black arrow are presented. Arrows are aligned with the twin longest axis. (For interpretation of the references to colour in this figure legend, the reader is referred to the web version of this article.)

experimental measurements are higher for the transverse direction due to either the available constraints during experiments or lack of having enough sensitivity to measure transverse movements (Abdolvand et al., 2015a; Oliver et al., 2004; Quinta da Fonseca et al., 2006).

4.2.2. Parent grain analysis

Variations of elastic strains, elastic lattice rotation, and stress during formation of twins M1T6 and M1T5 in their corresponding parent grains are shown in Fig. 6 and Fig. 7, respectively. In these two figures, the model M1T5&T6 was used to generate the results. Since the c-axis of both M1G4 and M1G3 are oriented toward the loading direction, a high elastic strain and stress are captured in this direction before twin reorientation (See Figs. 6a and 7a). However, the twin shear transfer results in significant stress relaxation in this direction (Figs. 6b and 7b). For the shear component, formation of M1T6 changes the sign of the shear stress and elastic strain fields at the area close to the two ends of the twin. However, rotation fields are not altered much except for Ω_{12}^{el} (compare Fig. 6a and b).

Results at the end of unload phase for the case where no twin is simulated and the case where the twins M1T5 and M1T6 are inserted into the model are presented in Fig. 6c and d, for comparison. It is clear from this comparison that twin formation had significant influence on elastic strains and stress particularly in the ϵ_{11} , σ_{11} and ϵ_{12} , σ_{12} components. Similar to what presented in Fig. 6b, rotation fields are not changed much except for Ω_{12}^{el} within the twin domain. A direct comparison between CPFE and HR-EBSD are also given in Fig. 6e and f. Since M1T6 cut through M1G4, three grains are identified and three reference points are used for HR-EBSD calculation. For this case, the CPFE results for relative strain calculations are very different to the actual calculated one presented in Fig. 4d. CPFE and HR-EBSD results indicate a high positive relative stress and elastic strain on the right hand side of M1G4 in the x_1 direction, however in the left hand side of M1G4, they are small and uniform. For the shear components, both CPFE and HR-EBSD show a positive shear stress and strain in the south part of M1T6 and a negative stress in the north part. In Fig. 6a to d it is shown that the observed variation in ϵ_{12}^{el} and σ_{12} are a result of twin shear transfer.

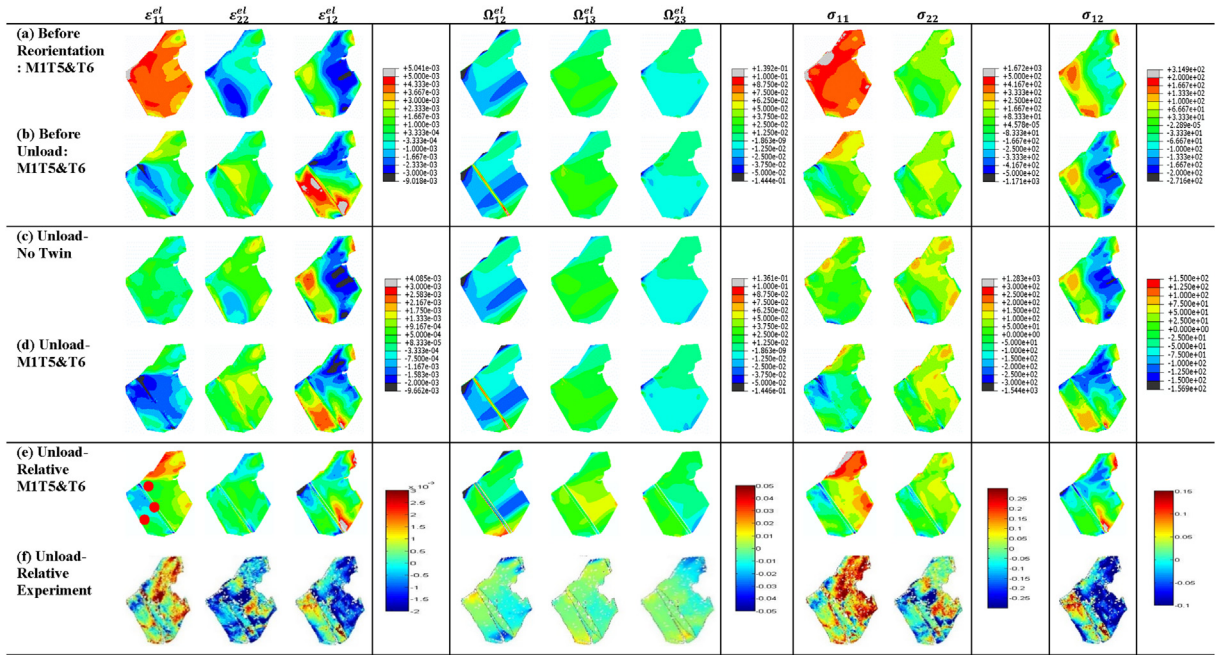


Fig. 6. Comparison between different model and assumptions for the grain M1G4: each model label is given in the first column, elastic strains are given in the second to the fourth column with the corresponding colour bar given in fifth column. Elastic lattice rotations are given in the sixth to the eighth column with the corresponding colour bar in the ninth column. Lattice rotations are given in radian. Normal stresses are given in the tenth and eleventh column with the corresponding colour bar given in the twelfth column. Shear strain and the related colour bars are given in the last two columns. Stresses are given in MPa and 11 coincides with the loading direction and 22 is the transverse direction (see Fig. 1b). The results of HR-EBSD are given in the last column (f) whereas the CPFE results with reference point reduced are presented in the rest. These reference points are shown with red dots in (e). (For interpretation of the references to colour in this figure legend, the reader is referred to the web version of this article.)

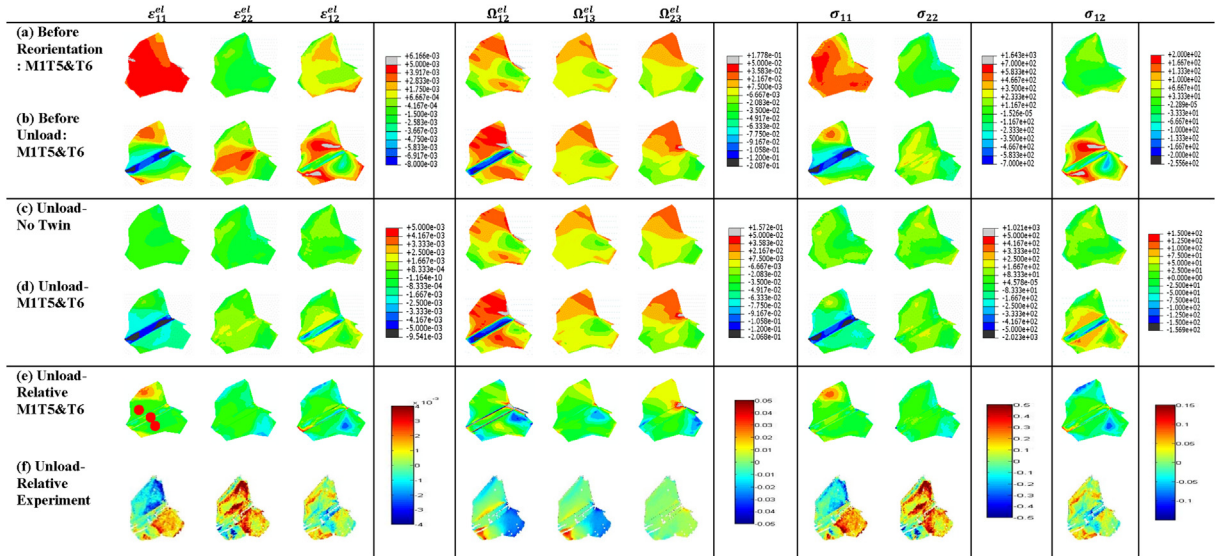


Fig. 7. Comparison between different model and assumptions for the grain M1G3: each model label is given in the first column, elastic strains are given in the second to the fourth column with the corresponding colour bar given in fifth column. Elastic lattice rotations are given in the sixth to the eighth column with the corresponding colour bar in the ninth column. Lattice rotations are given in radian. Normal stresses are given in the tenth and eleventh column with the corresponding colour bar given in the twelfth column. Shear strain and the related colour bars are given in the last two columns. Stresses are given in MPa and 11 coincides with the loading direction and 22 is the transverse direction (see Fig. 1b). The results of HR-EBSD are given in the last column whereas the CPFE results with reference point reduced are presented in the rest. These reference points are shown with red dots in (e). (For interpretation of the references to colour in this figure legend, the reader is referred to the web version of this article.)

The CPFE results shown in Fig. 7c and d indicate that at unload, M1T5 do not really alter the longitudinal (σ_{11}) and transverse (σ_{22}) residual stresses within M1G3 except for the area close the twin boundary. However, a big difference is observed for the shear stress component (σ_{12}). The relative stress and elastic strain for this grain is shown in Fig. 7e and f. Similar to M1G4, three reference points are used in calculating relative values; these reference points are indicated with red circles in Fig. 7e. For this grain, the CPFE results for relative stress and elastic strain do not really match with the experimental ones. For instance, in Fig. 6d it is shown that in the north part of M1G3, at the boundary shared with M1T5, a negative elastic strain and stress exist at the unload case. Since the corresponding reference point is located in this area, a positive relative stress and strain are captured in CPFE calculation in the north part of M1G3. In the discussion we will show that some of these discrepancies are actually originating from the assumption we made for the stage at which twin nucleated, i.e. M1T5 was nucleated long before the applied strain reaches 2.7%. Although the captured rotation fields from CPFE are not far away from experiment, it will be shown in Section 5.3 that if twin M1T5 nucleates at the applied strain of 1%, a much better agreement could actually be achieved.

5. Discussion

5.1. State of the twin and elastic energy

In all of the figures presented in Section 4, it was assumed that state of stress within twin at its inception is zero. This assumption was used since a previous study of lattice strain evolution during twin formation in Mg alloys indicated a huge relaxation within the twin (Brown et al., 2005; Clausen et al., 2008). Such experimental observation has led to assignment of zero stress to newly nucleated twins in crystal plasticity codes developed for self-consistent framework (Abdolvand and Daymond, 2012; Juan et al., 2014). One should note that in a self-consistent code, the actual interaction between twin and parent is missed since each grain interacts with the homogenous medium representing all grains except the one that is modelled. However, in a finite element framework a more “realistic” study of such local interaction can be carried out. In this section and the following one, effects of twin reorientation and twin stress state at the nucleation phase is discussed.

We first start with an examination of the elastic (strain) energy terms. The elastic energy per unit volume is calculated using the following equation:

$$E = \frac{1}{2} \sigma_{ij} \epsilon_{ij}^{el} \quad (10)$$

In Fig. 8 the evolution of elastic energy within three modelled parent/twin pairs are shown. These elastic energies are the average values calculated over all of the IPs that fall into the parent or twin domains. It is shown in Fig. 8a that elastic energy within grain M1G4 increases from zero to 1 MJ/m³ during loading phase. The three curves are shown for the rest of the phases represent average elastic energy within the twin domain (purple line), average elastic energy within parent that is excluded from that of twin (red line), and the weighted-average energy of both twin and parent domains combined (blue line). At the reorientation phase, the energy of M1T6 drops as a result of both assigning zero stress and reorienting the twin domain which lowers the stiffness along the extension axis (x_1). In Section 5.2, it is shown that since this twin is embedded within the parent grain, FE results shows that the stress within the twin immediately returns to higher values to re-equilibrate the local stresses. That is why a U-shape curve is captured for energy of M1T6 during reorientation. While elastic energy of M1G4 and total elastic energy do not significantly change during reorientation, a big drop is observed during the first 200 steps of TST. This indicates that twin shear transfer plays a major role in dropping the total elastic energy of the system. After step = 400, the elastic energy of M1G4 does not radically change; therefore, it is energetically more favourable for M1G4 to nucleate another twin rather than having M1T6 grown or thicken. This is probably why two more needle-like twins are nucleated and propagated within this grain (Fig. 1c), assuming that twin surface energy does not play significant role.

A similar trend is also observed for the M1G2/M1T1 pair. It is shown in Fig. 8b that the twin shear transfer plays major role in reduction of elastic energy of the system. However after step = 400 this energy does not change significantly. This could probably encourage formation of the other three twins in M1G2. Trends observed for M1G3/M1T5 are rather different. Since, M1T5 is much bigger than the other two modelled twins, the energy drop within the twin at the reorientation phase is much bigger. Further, although the constraint imposed at the twin/parent shared boundaries reinforce force equilibrium, due its size, a stress gradient does exist through M1T5 thickness. Interestingly, the energy of the twin/parent system decreased during both reorientation and TST, but after step = 400, increases again which means that it is not energetically favourable to thicken this twin; this is the probable reason why M1T5 is a double twin, i.e. two thinner twin of the same variant are formed rather than a big thick one (see Fig. 1c). This is also compatible with the report given by Zhang et al. (2008) that 3 micron twin thickness is the optimum value to reduce the elastic energy of the parent grain.

In Fig. 8d and e the effects of twin reorientation and initial stress state of the twin on the calculated average elastic energy within M1G4/M1T6 pair are illustrated. For the models RE0 and REN0, the average energy of the system decreases with or without setting initial stress of twin to zero. The rapid increase in the elastic energy of the twin in the model REN0 is mostly due to calculating higher stresses as a result of deactivating slip within the twin domain. If the twin reorientation is turned off, the average elastic energy of the system still decreases during the TST phase (Fig. 8e), however, the elastic energy of the twin domain increases rapidly after step = 400. The comparison between these four models highlights the dominant effect of TST on the reducing average elastic energy of the twin/parent pairs.

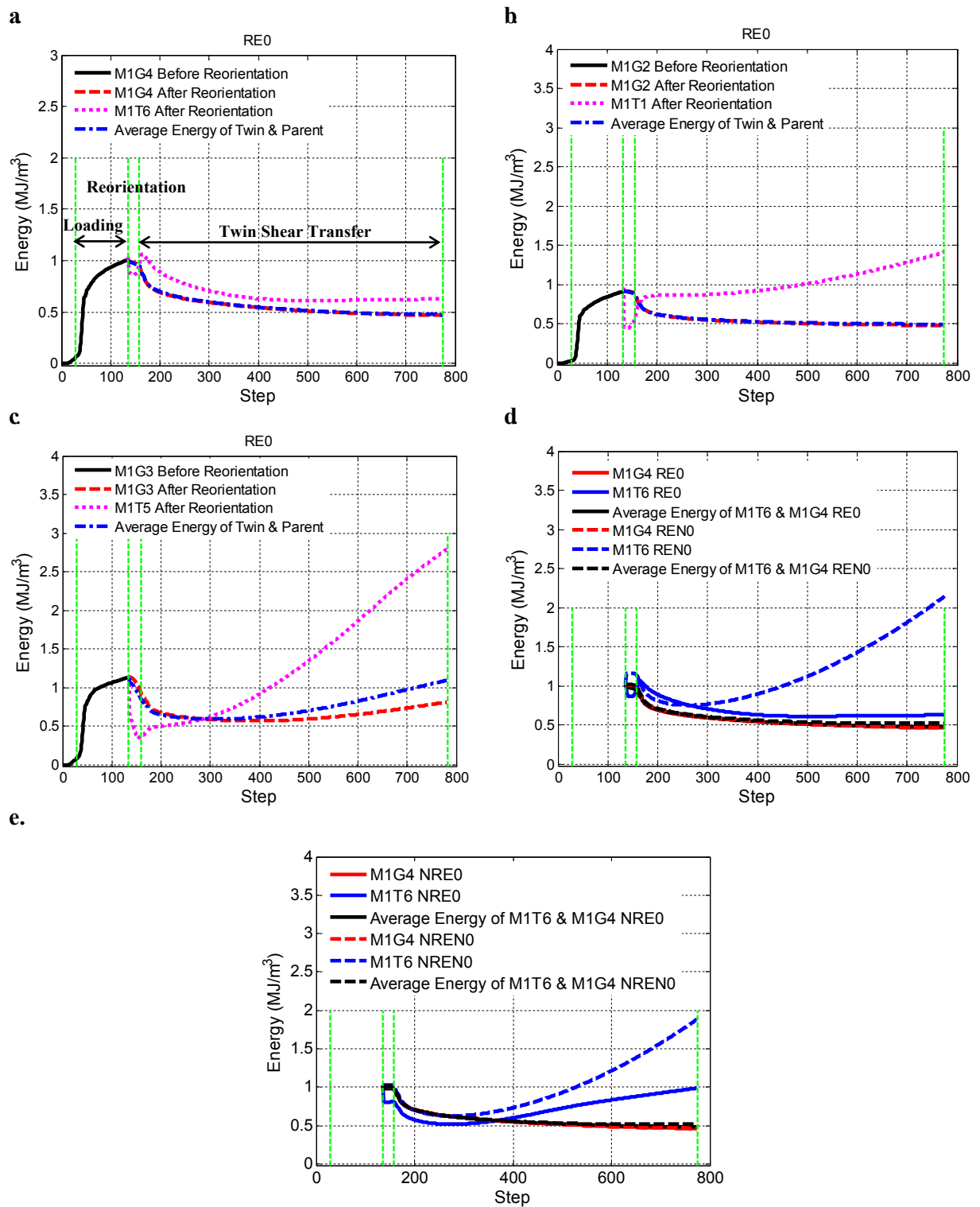


Fig.8. Evolution of elastic energy in the modelled twin and parent pairs: (a) for M1G4/M1T6 pair, (b) M1G2/M1T1 pair, (c) M1G3/M1T5 pair; in (a) to (c) stress at the twin inception was set to zero (RE0 assumption). Effects of various assumption on the elastic energy evolution in M1G4/M1T6 pair: (d) RE0 vs REN0 and (e) NRE0 vs NRNO.

5.2. Evolution of average stress of twin and parent pairs

In Section 4.2 a direct comparison between CPFE and HR-EBSD results are provided where relative stress and elastic strain fields are compared in detail. The advantage of such comparison is that spatial distribution of relative values can be compared and a better insight to the deformation mechanism can be provided. Here, the CPFE results are compared against another experimental source, of 3D synchrotron X-ray diffraction (3DXRD) data previously published by Abdolvand et al. on the same material (Abdolvand et al., 2015b, c). A comprehensive explanation of 3DXRD technique is given in (Poulsen, 2004; Poulsen et al., 2001). In a 3DXRD experiment, average stress over an entire grain can be measured *in-situ* in 3D, hence in what follows the evolution of average stress within twin and parent pairs are compared against experimental data.

In Fig. 9 the evolution of stress in the M1G4/M1T6 pair is illustrated using RE0 assumption in (a) to (c) and RENO assumption in (d) to (f). It is shown in Fig. 9a that the average in-plane stresses of M1G4 increase during the loading phase. For

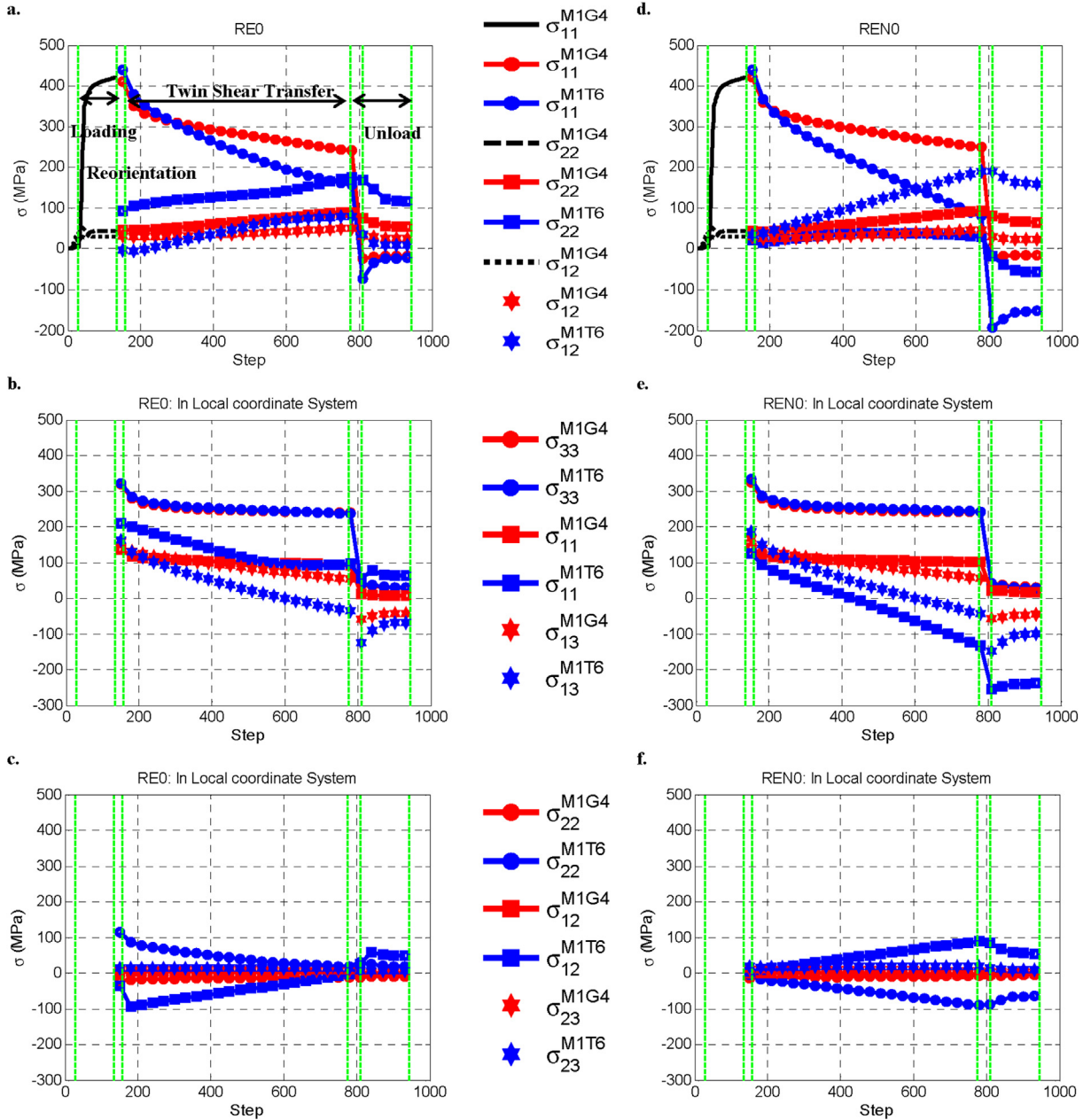


Fig. 9. Evolution of average stress within M1G4 and M1T6 with stress within twin set to zero at the inception: (a) in global coordinate system, (b) and (c) are given in local twin coordinate system. Same results with non-zero stress assigned to twin at the inception are shown in (d) and are in global coordinate system; (e) and (f) are given in the local twin coordinate system.

instance, σ_{11} increase to 430 MPa after which this curve divides into two others that represent average stress within M1G1 domain (red curves) and average stress over M1T6 (blue curves). In agreement with the studies performed on single crystals, stress in the loading direction decreases during twinning (Cote et al., 2015; Eisenlohr et al., 2012). Comparison between Fig. 9a and d indicates that regardless of the twin's state of stress at nucleation, the twin shear transfer controls such reduction in the stress in the loading direction. In Fig. 9b and c the evolution of average stress in the local twin coordinate system is shown. As stated in Section 4, the local twin coordinate system is defined in the way that x_1 coincides with twin shear direction and x_3 with the normal to the twin habit plane. In Fig. 9b it is shown that the average σ_{33}^{local} in the twin and parent are the same through the reorientation and TST phases; interestingly, twin shear transfer results in smaller σ_{13}^{local} within the twin in comparison to the parent. These trends are observed for REN0 case (Fig. 9e). It is shown that with RE0 assumption σ_{11}^{local} in the twin is higher than that of the parent grain.

While Fig. 9b and e shows the in-plane stress in the twin local coordinate system, Fig. 9c and f shows out-of-plane components. It is worth mentioning that a better explanation of the out-of-plane components can be given by a fully 3D simulation. Nevertheless, it is shown that out-of-plane shear components are quite small and negligible comparing to the in-plane shear component (σ_{13}^{local}).

To provide more evidence on how twin-parent stresses are related, the average in-plane stresses of M1G3/M1T4 as well as M1G2/M1T1 pair in the twin local coordinate system is shown in Fig. 10a and b. It is shown in both cases that stress normal to the twin habit plane in the twin and parent are the same through the reorientation and TST phases whereas in the twin shear direction, stress (σ_{13}^{local}) within twin is smaller than that of the parent. For this two pairs, in contrast to the M1G4/M1T6 pair, the average σ_{11}^{local} in the parent is higher than that of the twin.

In Fig. 10c and d, stresses in the twins as a function of the corresponding stresses in parent grain that were measured by 3DXRD are illustrated. These data were measured with the sample under in-situ loading at 2.7% uniaxial strain applied to the same material studied here and give the average stress over entire twin or parent grain (Abdolvand et al., 2015b, c). In these figures smaller dots represent each individual twin/parent pair whereas the big dots represent the average value calculated

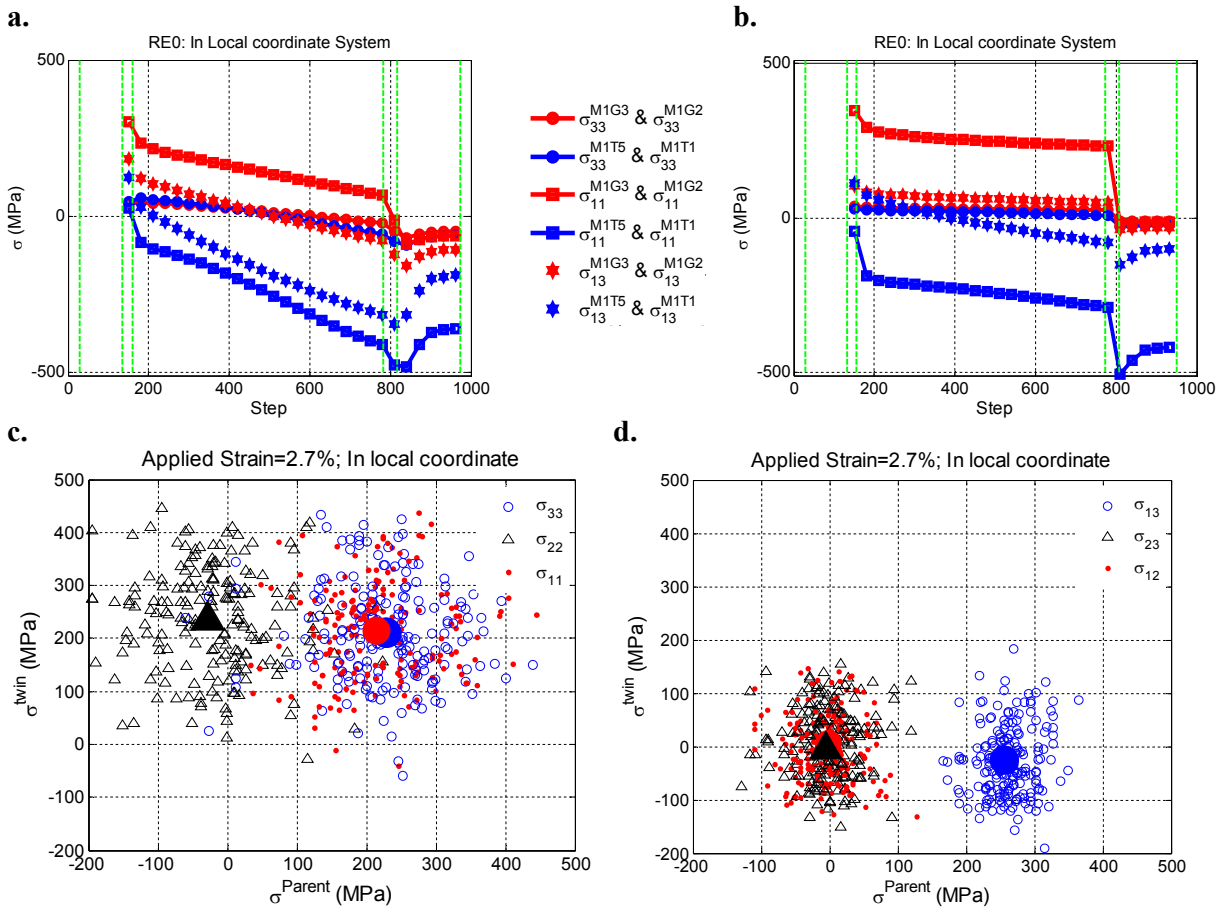


Fig. 10. Evolution of average stress in (a) M1G3/M1T5 pair and (b) M1G2/M1T1 pair with stress in twin set to zero at the inception. Measured average stress within twin as a function of measured average stress in the parent in the (c) normal components and (d) shear components (Abdolvand et al., 2015b, c). All of the results are given in the twin coordinate system. Smaller symbols represent each twin/parent pair whereas the big solid symbols represent average value of each data set over all of the measured twin/parent pairs.

for all of the twin/parent pairs measured during the experiment. For instance, each blue circle in Fig. 10c represents the relationship between σ_{33}^{local} of each twin and parent whereas the big blue dot represents the average value calculated for all of the measured twin/parent pairs. In agreement with the 3DXRD results, it is shown that for the modelled twins, σ_{33}^{local} in the twin and parent are the same, whereas σ_{33}^{local} in the parent is higher than that of the twin. These trends are also observed in twin/parent pairs of MgAZ31B (Abdolvand et al., 2015a). The reason for the observed trends is that, force equilibrium reinforces equal σ_{33}^{local} across the twin boundary. If the twin is thin, a uniform stress in the local x_3' will develop and hence the average σ_{33}^{local} in the twin and parent will be the same. For the shear direction, it is shown here that the TST plays a significant role in the twin/parent load sharing. This is in agreement with other recent numerical studies carried out on formation of twins in Mg alloys (Kumar et al., 2015). It is worth mentioning that since twinning is a polarized process, σ_{13}^{local} in the parent has to be positive through the twin formation as it provides positive driving force for twin nucleation. Also, the zirconium elastic anisotropy is responsible for smaller calculated or measured σ_{23}^{local} or σ_{12}^{local} (see Figs. 9c and 10d). The relationship calculated for stress components within twin and parent pairs modelled and presented in this section, all fall into the cloud of the data measured using 3DXRD.

5.3. Effects of twin nucleation stage

In the present study, we focused on the effect of reorientation and TST during twin formation; however, the effect of twin nucleation and thickening on our results were neglected. Generally, it is difficult to determine the applied macroscopic strain at which twin nucleation takes place, since an ex-situ HR-EBSD experiment was performed here. To examine the effects of the timing of twin inception on the results presented in Figs. 4, 6 and 7, two different case studies are presented. The model MIT5&T6 was used to simulate reorientation and TST during M1T5 and M1T6 formation. For the first case, twin reorientation was implemented at $\epsilon_{applied} = 1\%$ as opposed to $\epsilon_{applied} = 2.7\%$ that was used before. The TST for case-I was also assumed to take place under constant applied strain. After TST phase, the sample was uniaxially strained up to 2.7% and then unloaded to compare the results to those presented in Section 4. For the case-II, twin reorientation was implemented at $\epsilon_{applied} = 2.7\%$ which was followed by a TST phase under constant applied strain. After TST, the sample strained up to 4% and then unloaded. For the both cases it was assumed that the twins do not thicken and the size of the twins are the same as those modelled in Section 4 and presented in Fig. 1g.

In comparison to what is presented in Fig. 4f, applying more strain to the model results in higher Ω_{12}^{el} and Ω_{13}^{el} rotation intensity close to both M1T5 and M1T6 (see Fig. 11a and b), however Ω_{23}^{el} has not changed much. A closer agreement to HR-EBSD results would be achieved for ϵ_{11}^{el} and σ_{11} since higher compressive values are calculated in both case-I and case-II, however ϵ_{22}^{el} and σ_{22} are not changed much for which the discrepancy between HR-EBSD and CPFE still stands.

It is shown in Fig. 11c and d that with applying load after the TST phase, while elastic lattice rotations do not change significantly, elastic strains and stresses in M1G4 change significantly comparing to those presented in Fig. 6d. This follows with much better agreement with HR-EBSD results presented in Fig. 6f. For instance, with applying more strain after the TST phase, the sign of ϵ_{11}^{el} and σ_{11} in the right hand side of M1G1 changes from compressive to tensile while at the reference point they stay negative. This results in positive relative ϵ_{11}^{el} and σ_{11} which are in closer agreement with HR-EBSD results. The same trend is also captured for ϵ_{12}^{el} where better agreement with HR-EBSD measurements results.

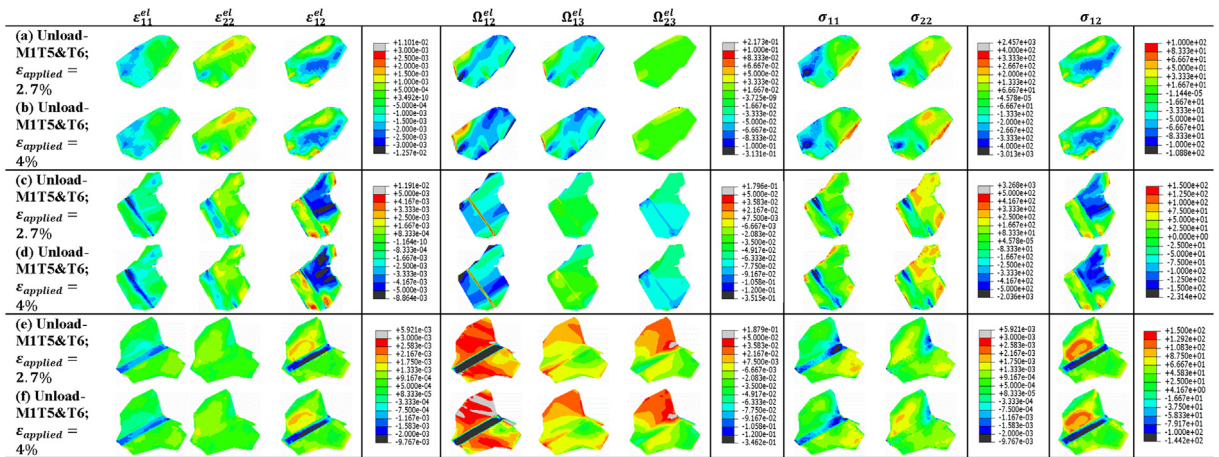


Fig. 11. CPFE results for examining the effects of nucleating twins at different applied strains. Results for M1G1 are represented in the first two columns followed by those for M1G4, and M1G3; elastic strains are given in the second to the fourth column with the corresponding colour bar given in fifth column. Elastic lattice rotations are given in the sixth to the eighth columns with the corresponding colour bar in the ninth columns. Lattice rotations are given in radian. Normal stresses are given in the tenth and eleventh column with the corresponding colour bar given in the twelfth column. Shear strain and the related colour bar are given in the last two columns. Stresses are given in MPa and 11 coincides with the loading direction and 22 is the transverse direction (see Fig. 1b). The case $\epsilon_{applied} = 2.7\%$ and $\epsilon_{applied} = 4\%$ represent case-I and case-II where total strain of 2.7 and 4% are applied, respectively.

In Fig. 11e and f the result of case-I and case-II for M1G3/M1T5 pair is presented. In comparison to Fig. 7d, with applying strain after the TST phase, the magnitude of compressive ϵ_{11}^{el} close to twin boundary decreases for case-I and even vanishes completely for case-II. Again the result is in better agreement with HR-EBSD measurements for the north part of M1G3. For the shears, a crescent of high positive ϵ_{12}^{el} in the north part of M1G3 is achieved which is different to that presented in Fig. 7d. This crescent is also seen in the HR-EBSD results. Similar to the other two grains studied above, the calculated elastic strain in the transverse direction is not changed a lot.

5.4. The implemented approach and sources of discrepancies

Various assumptions were made in the body of the crystal plasticity code that were used in this study. Following the fast Fourier transformation framework that was suggested recently by Kumar et al. (2015), the TST was modelled as a plastic shear that acts on the twin domain. The advantage of this model is that, since the “real” grain structure is imported to ABAQUS, a “real” interaction between the twin and the surrounding environment can be captured. For instance, the effects of the back stresses on the state of the twin at the nucleation stage has been studied in detail using a self-consistent framework (Clausen et al., 2008), but with the current approach, such interaction will naturally be imposed on the twin by the FE solver. Another approach is to apply TS as an external boundary condition acting on the habit plane; however, with this approach part of the applied TS will be accommodated as elastic strain within the twin domain. With this approach, Zhang et al. (2008) have shown that during twin formation stress in the parent grain drops which is in agreement with what is reported in this paper. Also, we neglected the effects of twin thickening on the state of stress within twin and parent. Zhang et al. (2008) have shown that stress within the parent grain of a zirconium sample decreases as the volume fraction of the twin increases, however, in agreement with the recent study carried out by Ardeljan et al. (2015) and what is shown in Section 5.1, there is a limit to this where energetically it is favourable to have another twin within the parent grain rather than increasing the volume fraction of the current one.

Assuming that the reorientation and the TST approach presented in Section 3.1 is a reasonable approach to model twinning, there are several factors that can affect our calculation results that need to be addressed. Firstly, experimental observation have shown that at the nucleation and propagation stages, twins are in the form of thin lamella that subsequently thicken under the action of continued loading. An alternative approach to the one presented in this paper, might be the one where TS is applied to the thin lamella followed by twin thickening. The thickening stage can be a function of applied load where the thickness or the volume fraction of the twin can be calculated using a pseudo-slip equation (Houtte, 1978; Tomé et al., 1991). The authors of the current paper are developing such model. Secondly, it was assumed that TST happens over a long time interval, i.e. 3060 s; In contrast to the thickening stage, it is generally believed that twin nucleation and propagation are dynamic processes. Such effects are not included in the current study and they can potentially affect the state of the calculated stresses.

In Section 4.2, with the use of CPFE and HR-EBSD, it was shown that there are strain and stress gradients within twins and across twin boundaries. This is in agreement with the studies carried out on twins in Mg alloys with the use of differential-aperture X-ray microscopy (Balogh et al., 2013). To provide an upper bound, the TST was applied in the x-y plane and results were compared to the lower bound case where no twin exists. The three-dimensional nature of TST was not fully captured and this could cause changes in the magnitude of the calculated stresses. A first attempt at exploring this is documented in Appendix C. It is worth mentioning that modelling the 3D twin shear demands lots of element to accommodate the required deformation through the model thickness. Such model demands a much powerful machine to run simulations and it is not the scope of the current study. Also, the HR-EBSD technique measures the deformation state of the material at the free surface. The effects of sub-surface grains are neglected in CPFE simulation; it has been shown that they can potentially have significant influence on the calculated stresses and strains (St-Pierre et al., 2008; Zeghadi et al., 2007a, 2007b; Zhang et al., 2015).

Another source of discrepancies between the model and experiment might be in their abilities to capture discrete dislocation effects. Localized stress concentrations that are associated with pile-ups of dislocations cannot be modelled explicitly within the current CPFE code. Such effects can be studied to some extent with strain-gradient based CPFE codes (Dunne et al., 2007), but even these approaches homogenise some of the detail seen in the HR-EBSD data which can be linked to the discrete dislocation aspects of plasticity (Wilkinson et al., 2014). Within the CPFE framework, if it is intended to capture the sharp gradients that are associated with the pile-ups of dislocations, it is necessary to (a) include the stress and the deformation fields induced by each dislocation at each IP and (b) use very small elements to capture such gradients. Both of these are computationally costly. Furthermore, the accuracy of the HR-BESD measurements for elastic strains is a function of distortions of the EBSD detector optics, changes in the band asymmetry influenced by lattice rotation, and accurate determination of EBSD pattern centres (Jiang et al., 2013b). Improving the contribution of each of these terms into the final measurement is the scope of ongoing research conducted by the authors.

5.5. effects of other twins in the area

In Section 4.2, the effects of three modelled twins on the stress distribution of parent and neighbouring grains were presented. In these simulations, the effects of other twins in the area on the stress distributions are neglected. Inclusion of these twins could potentially alter the simulation results and be the source of discrepancies. To investigate this, the effects of three additional twins that impinge M1G1 were studied, i.e. effects of M1T2, M1T3, and M1T4 on the stress induced by M1T6

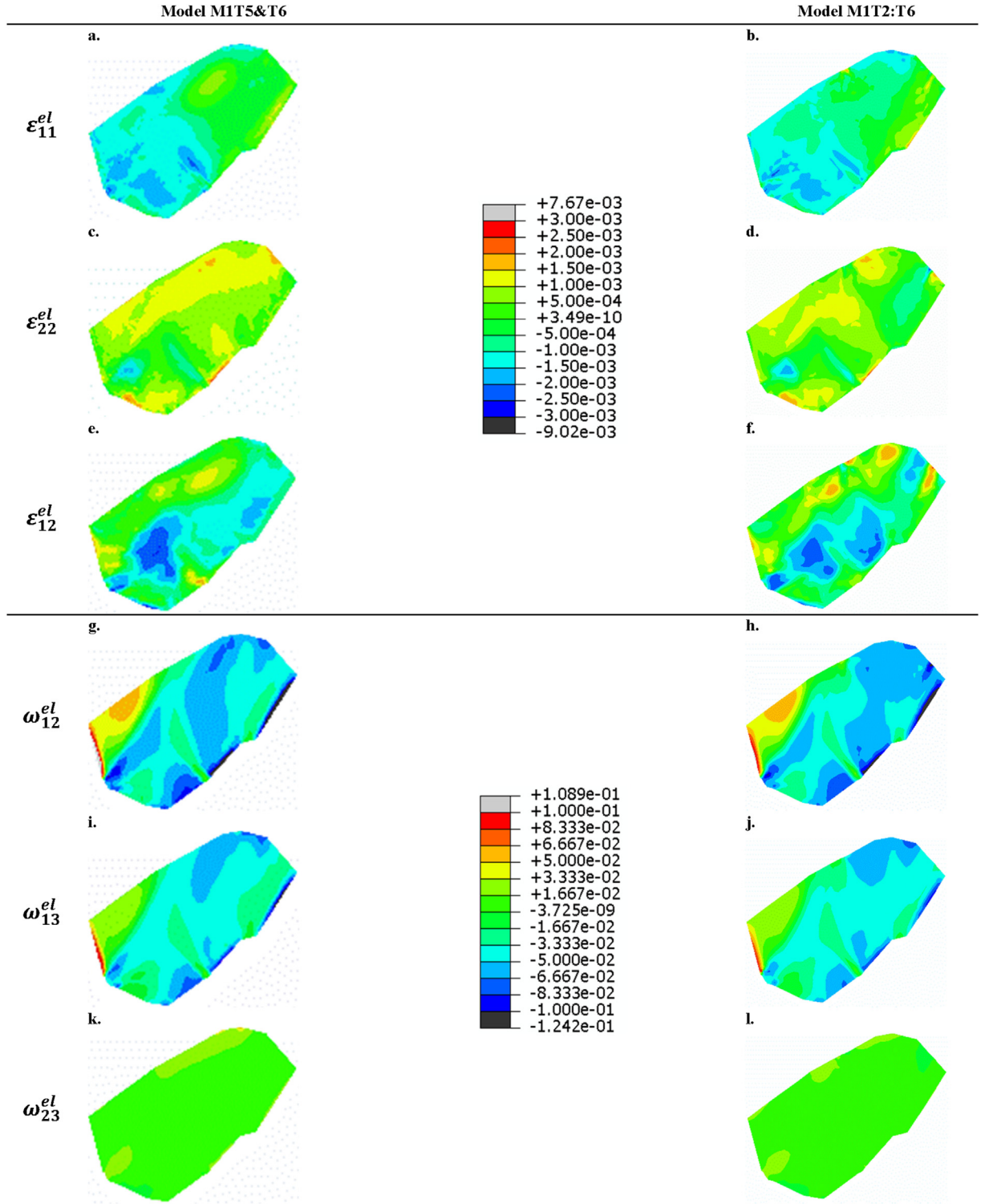


Fig.12. Comparison between results of the MIT5&T6 model with MIT2:T6 for the calculated elastic strain in (a) to (f) and calculated elastic lattice rotation in (g) to (l). Elastic rotations are given in radians.

and MIT5 within M1G1 (see Fig. 1a and c). As the sequence of nucleation of these twins is not known, they are all assumed to nucleate simultaneously. Similar to what was explained in Section 3.1 and 3.2, the twin domains were firstly reoriented and then twin shears applied over a 3060 s period. In Fig. 12, elastic strains and lattice rotations induced in M1G1 by all of the twins impinging on it (model MIT2:T6) are compared against those calculated using model MIT5&T6. The comparison

between the two shows that elastic strain and lattice rotation induced by M1T5 and M1T6 within M1G1 are not much affected by the nucleation of the additional twins M1T2:T4. Strain and rotation fields in the key areas close to the M1T5 and M1T6 tips within M1G1 are not changed very much however more significant changes are seen for the areas close to the intersection of M1T2:T4 with M1G1.

In the simulations presented in this paper, the effects of reorientation and TST during the formation of three twins were studied in detail, however there are many other twins within the simulated area the effects of which have been neglected. The authors are updating the CPFE code to be able to include reorientation and TST during nucleation of multiple twins and this will be the subject of future study.

6. Conclusions

The effects of reorientation and twin transformation strain on the state of stress within twin, parent and their associated neighbourhood was studied in detail using CPFEA simulations, HR-EBSD, and 3DXRD measurements. A Zircaloy-2 sample with HCP crystal structure was uniaxially strained in the direction that favours twinning and then unloaded for further analysis. Relative elastic surface strain, lattice rotation, and stress variations within several twin and parent grains were measured by the use of high resolution EBSD. The HR-EBSD provides the spatial distribution of residual stresses. To provide information regarding the status of the sample under load and to provide “true” strain, rotation, and stress values, the measured EBSD map was imported into ABAQUS CAE and modelled with a crystal plasticity finite element code. The CPFE code was modified to incorporate the effect of the twin transformation strain on the state of stress within the twin and parent.

Three twins were studied in detail. High stress and rotation concentrations were measured at the shared boundary of a soft grain with two neighbouring twins. The CPFE calculation indicated that the rotation and the stress fields were induced by the twin transformation strain imposed during formation of the twin in the neighbouring grain. The CPFE simulations show that in the parent grain the stress in the loading direction relaxes upon twin formation. Besides, the twin has a pronounced effect on re-distributing the rotation field, strain, and elastic stress. Good agreement was achieved between CPFE calculation and HR-EBSD measurement for lattice rotations particularly close to the twin tips. In terms of relative elastic strains and stresses, a better agreement was achieved in the loading direction.

It was shown that the elastic strain energy of the parent grain and the twinned domain combined generally decreases when the twin forms. It was shown that although reorientation and the state of the stress within twin can alter the elastic energy, the twin transformation strain plays the most significant role among the three. Also, various assumptions for the state of the stress within the twinned domain at the nucleation stage were tested. It was shown that if the initial state of the twin at nucleation is set to zero, as a result of reinforcing force equilibrium, a new stress will be immediately imposed within the twinned domain.

It was shown that between reorientation and twin transformation strain, the later has higher impact on the average stress within the parent grain. The CPFE simulation shows that this average stress in the loading direction reduces significantly as a result of twin shear transfer. A twin coordinate system was defined with x_1 direction coinciding with the twin shear direction and x_3 along the normal to the twin habit plane. In agreement with previously published data, CPFE results shows that the average σ_{33}^{local} are the same for twin and parent, however, the twin shear transfer results in smaller σ_{13}^{local} in the twin compared to within the parent.

Acknowledgements

The authors would like to acknowledge Prof. Mark Daymond for the provision of the Zircaloy sample. This work is part of the HEXMAT program funded by Engineering and Physical Sciences Research Council (EP/K034332/1). Data in support of this paper will be made accessible on the Oxford Research Archive (www.ora.ox.ac.uk) and Zenodo.org: <http://dx.doi.org/10.5281/zenodo.53977>.

Appendix A. Supplementary data

Supplementary data related to this article can be found at <http://dx.doi.org/10.1016/j.ijplas.2016.05.006>.

References

- Abaqus, 2014. Standars User's Manual Version 6.5. Habitt, Karllsson & Sorensen, Inc.
- Abdolvand, H., Daymond, M.R., 2012. Internal strain and texture development during twinning: comparing neutron diffraction measurements with crystal plasticity finite-element approaches. *Acta Mater.* 60, 2240–2248.
- Abdolvand, H., Daymond, M.R., 2013a. Multi-scale modeling and experimental study of twin inception and propagation in hexagonal close-packed materials using a crystal plasticity finite element approach—part I: average behavior. *J. Mech. Phys. Solids* 61, 783–802.
- Abdolvand, H., Daymond, M.R., 2013b. Multi-scale modeling and experimental study of twin inception and propagation in hexagonal close-packed materials using a crystal plasticity finite element approach; part II: local behavior. *J. Mech. Phys. Solids* 61, 803–818.
- Abdolvand, H., Daymond, M.R., Mareau, C., 2011. Incorporation of twinning into a crystal plasticity finite element model: evolution of lattice strains and texture in Zircaloy-2. *Int. J. Plasticity* 27, 1721–1738.
- Abdolvand, H., Majkut, M., Oddershede, J., Schmidt, S., Lienert, U., Diak, B.J., Withers, P.J., Daymond, M.R., 2015a. On the deformation twinning of Mg AZ31B: a three-dimensional synchrotron X-ray diffraction experiment and crystal plasticity finite element model. *Int. J. Plasticity* 70, 77–97.

- Abdolvand, H., Majkut, M., Oddershede, J., Wright, J.P., Daymond, M.R., 2015b. Study of 3-D stress development in parent and twin pairs of a hexagonal close-packed polycrystal: part I – in-situ three-dimensional synchrotron X-ray diffraction measurement. *Acta Mater.* 93, 246–255.
- Abdolvand, H., Majkut, M., Oddershede, J., Wright, J.P., Daymond, M.R., 2015c. Study of 3-D stress development in parent and twin pairs of a hexagonal close-packed polycrystal: part II – crystal plasticity finite element modeling. *Acta Mater.* 93, 235–245.
- Abdolvand, H., Wilkinson, A.J., 2016. Assessment of residual stress fields at deformation twin tips and the surrounding environments. *Acta Mater.* 105, 219–231.
- Agnew, S.R., Duygulu, Ö., 2005. Plastic anisotropy and the role of non-basal slip in magnesium alloy AZ31B. *Int. J. Plasticity* 21, 1161–1193.
- Ardelean, M., McCabe, R.J., Beyerlein, I.J., Knezevic, M., 2015. Explicit incorporation of deformation twins into crystal plasticity finite element models. *Comput. Methods Appl. Mech. Eng.* 295, 396–413.
- Arul Kumar, M., Kanjarla, A.K., Niezgoda, S.R., Lebensohn, R.A., Tomé, C.N., 2015. Numerical study of the stress state of a deformation twin in magnesium. *Acta Mater.* 84, 349–358.
- Asaro, R.J., 1983. Crystal plasticity. *J. Appl. Mech.* 50, 921–934.
- Asaro, R.J., Needleman, A., 1985. Overview no. 42 Texture development and strain hardening in rate dependent polycrystals. *Acta Metall.* 33, 923–953.
- Balogh, L., Niezgoda, S.R., Kanjarla, A.K., Brown, D.W., Clausen, B., Liu, W., Tomé, C.N., 2013. Spatially resolved in situ strain measurements from an interior twinned grain in bulk polycrystalline AZ31 alloy. *Acta Mater.* 61, 3612–3620.
- Barnett, M.R., 2007. Twinning and the ductility of magnesium alloys: part II. “Contraction” twins. *Mater. Sci. Eng. A* 464, 8–16.
- Barnett, M.R., Stanford, N., Ghaderi, A., Siska, F., 2013. Plastic relaxation of the internal stress induced by twinning. *Acta Mater.* 61, 7859–7867.
- Beyerlein, I.J., Capolungo, L., Marshall, P.E., McCabe, R.J., Tomé, C.N., 2010. Statistical analyses of deformation twinning in magnesium. *Philos. Mag.* 90, 2161–2190.
- Britton, B.T., Wilkinson, A.J., 2012a. Stress fields and geometrically necessary dislocation density distributions near the head of a blocked slip band. *Acta Mater.* 60, 5773–5782.
- Britton, T.B., Jiang, J., Clough, R., Tarleton, E., Kirkland, A.I., Wilkinson, A.J., 2013. Assessing the precision of strain measurements using electron backscatter diffraction – part 1: detector assessment. *Ultramicroscopy* 135, 126–135.
- Britton, T.B., Wilkinson, A.J., 2012b. High resolution electron backscatter diffraction measurements of elastic strain variations in the presence of larger lattice rotations. *Ultramicroscopy* 114, 82–95.
- Brown, D.W., Agnew, S.R., Bourke, M.A.M., Holden, T.M., Vogel, S.C., Tomé, C.N., 2005. Internal strain and texture evolution during deformation twinning in magnesium. *Mater. Sci. Eng. A* 399, 1–12.
- Brown, D.W., Beyerlein, I.J., Sisineros, T.A., Clausen, B., Tomé, C.N., 2012. Role of twinning and slip during compressive deformation of beryllium as a function of strain rate. *Int. J. Plasticity* 29, 120–135.
- Capolungo, L., Marshall, P.E., McCabe, R.J., Beyerlein, I.J., Tomé, C.N., 2009. Nucleation and growth of twins in Zr: a statistical study. *Acta Mater.* 57, 6047–6056.
- Chang, Y., Kochmann, D.M., 2015. A variational constitutive model for slip-twinning interactions in hcp metals: application to single- and polycrystalline magnesium. *Int. J. Plasticity* 73, 39–61.
- Cheng, J., Ghosh, S., 2015. A crystal plasticity FE model for deformation with twin nucleation in magnesium alloys. *Int. J. Plasticity* 67, 148–170.
- Choi, W.S., De Cooman, B.C., Sandlöbes, S., Raabe, D., 2015. Size and orientation effects in partial dislocation-mediated deformation of twinning-induced plasticity steel micro-pillars. *Acta Mater.* 98, 391–404.
- Clausen, B., Tomé, C.N., Brown, D.W., Agnew, S.R., 2008. Reorientation and stress relaxation due to twinning: modeling and experimental characterization for Mg. *Acta Mater.* 56, 2456–2468.
- Cote, A.S., Darkins, R., Duffy, D.M., 2015. Deformation twinning and the role of amino acids and magnesium in calcite hardness from molecular simulation. *Phys. Chem. Chem. Phys.* 17, 20178–20184.
- Diard, O., Leclercq, S., Rousselier, G., Cailletaud, G., 2005. Evaluation of finite element based analysis of 3D multicrystalline aggregates plasticity: application to crystal plasticity model identification and the study of stress and strain fields near grain boundaries. *Int. J. Plasticity* 21, 691–722.
- Dunne, F.P.E., Rugg, D., Walker, A., 2007. Lengthscale-dependent, elastically anisotropic, physically-based hcp crystal plasticity: application to cold-dwell fatigue in Ti alloys. *Int. J. Plasticity* 23, 1061–1083.
- Eisenlohr, A., Gutierrez-Urrutia, I., Raabe, D., 2012. Adiabatic temperature increase associated with deformation twinning and dislocation plasticity. *Acta Mater.* 60, 3994–4004.
- Fisher, E.S., Renken, C.J., 1964. Single-crystal elastic moduli and the HCP–BCC transformation in Ti, Zr, and Hf. *Phys. Rev. B* 135, 482–494.
- Gong, J., Benjamin Britton, T., Cuddihy, M.A., Dunne, F.P.E., Wilkinson, A.J., 2015. (a) Prismatic, (a) basal, and (c+a) slip strengths of commercially pure Zr by micro-cantilever tests. *Acta Mater.* 96, 249–257.
- Guo, Y., Britton, T.B., Wilkinson, A.J., 2014. Slip band–grain boundary interactions in commercial-purity titanium. *Acta Mater.* 76, 1–12.
- Houtte, P.V., 1978. Simulation of the rolling and shear texture of brass by the Taylor theory adapted for mechanical twinning. *Acta Metall.* 26, 591–604.
- Izadbakhsh, A., Inal, K., Mishra, R.K., Niewczas, M., 2011. New crystal plasticity constitutive model for large strain deformation in single crystals of magnesium. *Comput. Mater. Sci.* 50, 2185–2202.
- Jiang, J., Britton, T.B., Wilkinson, A.J., 2013a. Evolution of dislocation density distributions in copper during tensile deformation. *Acta Mater.* 61, 7227–7239.
- Jiang, J., Britton, T.B., Wilkinson, A.J., 2013b. Mapping type III intragranular residual stress distributions in deformed copper polycrystals. *Acta Mater.* 61, 5895–5904.
- Jiang, J., Britton, T.B., Wilkinson, A.J., 2013c. Measurement of geometrically necessary dislocation density with high resolution electron backscatter diffraction: effects of detector binning and step size. *Ultramicroscopy* 125, 1–9.
- Jiang, J., Britton, T.B., Wilkinson, A.J., 2015. The orientation and strain dependence of dislocation structure evolution in monotonically deformed polycrystalline copper. *Int. J. Plasticity* 69, 102–117.
- Juan, P.A., Berbenni, S., Barnett, M.R., Tomé, C.N., Capolungo, L., 2014. A double inclusion homogenization scheme for polycrystals with hierarchical topologies: application to twinning in Mg alloys. *Int. J. Plasticity* 60, 182–196.
- Kalidindi, S.R., 1998. Incorporation of deformation twinning in crystal plasticity models. *J. Mech. Phys. Solids* 46, 267–290.
- Karamched, P.S., Wilkinson, A.J., 2011. High resolution electron back-scatter diffraction analysis of thermally and mechanically induced strains near carbide inclusions in a superalloy. *Acta Mater.* 59, 263–272.
- Kauffmann, A., Freudenberger, J., Geissler, D., Yin, S., Schillinger, W., Sarma, V.S., Bahmanpour, H., Scattergood, R., Khoshkhou, M.S., Wendrock, H., Koch, C.C., Eckert, J., Schultz, L., 2011. Severe deformation twinning in pure copper by cryogenic wire drawing. *Acta Mater.* 59, 7816–7823.
- Knezevic, M., Beyerlein, I.J., Brown, D.W., Sisineros, T.A., Tomé, C.N., 2013a. A polycrystal plasticity model for predicting mechanical response and texture evolution during strain-path changes: application to beryllium. *Int. J. Plasticity* 49, 185–198.
- Knezevic, M., Lebensohn, R.A., Cazacu, O., Revil-Baudard, B., Proust, G., Vogel, S.C., Nixon, M.E., 2013b. Modeling bending of α -titanium with embedded polycrystal plasticity in implicit finite elements. *Mater. Sci. Eng. A* 564, 116–126.
- Lim, H., Carroll, J.D., Battaile, C.C., Buchheit, T.E., Boyce, B.L., Weinberger, C.R., 2014. Grain-scale experimental validation of crystal plasticity finite element simulations of tantalum oligocrystals. *Int. J. Plasticity* 60, 1–18.
- Marko Knezevic, Mark R. Daymond, Irene J. Beyerlein, 2016, Modeling discrete twin lamellae in a microstructural framework, *Scripta Mater.*, in press, doi:10.1016/j.scriptamat.2016.04.026
- Máthis, K., Csizsár, G., Capek, J., Gubicza, J., Clausen, B., Lukáš, P., Vinogradov, A., Agnew, S.R., 2015. Effect of the loading mode on the evolution of the deformation mechanisms in randomly textured magnesium polycrystals – comparison of experimental and modeling results. *Int. J. Plasticity* 72, 127–150.

- Morrow, B.M., Lebensohn, R.A., Trujillo, C.P., Martinez, D.T., Addessio, F.L., Bronkhorst, C.A., Lookman, T., Cerreta, E.K., Characterization and modeling of mechanical behavior of single crystal titanium deformed by split-Hopkinson pressure bar. *Int. J. Plasticity* July 2016;82:225–240.
- Müllner, P., Solenthaler, C., Uggowitzer, P.J., Speidel, M.O., 1994. Brittle fracture in austenitic steel. *Acta Metallurgica Mater.* 42, 2211–2217.
- Muránsky, O., Carr, D.G., Sittner, P., Oliver, E.C., 2009. In situ neutron diffraction investigation of deformation twinning and pseudoelastic-like behaviour of extruded AZ31 magnesium alloy. *Int. J. Plasticity* 25, 1107–1127.
- Muránsky, O., Daymond, M.R., Bhattacharyya, D., Zanellato, O., Vogel, S.C., Edwards, L., 2013a. Load partitioning and evidence of deformation twinning in dual-phase fine-grained Zr–2.5%Nb alloy. *Mater. Sci. Eng. A* 564, 548–558.
- Muránsky, O., Daymond, M.R., Bhattacharyya, D., Zanellato, O., Vogel, S.C., Edwards, L., 2013b. Load partitioning and evidence of deformation twinning in dual-phase fine-grained Zr–2.5%Nb alloy. *Mater. Sci. Eng. A* 564, 548–558.
- Musienko, A., Tatschl, A., Schmidegg, K., Kolednik, O., Pippan, R., Cailletaud, G., 2007. Three-dimensional finite element simulation of a polycrystalline copper specimen. *Acta Mater.* 55, 4121–4136.
- Oliver, E.C., Daymond, M.R., Withers, P.J., 2004. Interphase and intergranular stress generation in carbon steels. *Acta Mater.* 52, 1937–1951.
- Ovid'ko, I.A., Sheinerman, A.G., 2014. Nanoscale cracks at deformation twins stopped by grain boundaries in bulk and thin-film materials with nanocrystalline and ultrafine-grained structures. *J. Phys. D Appl. Phys.* 47, 015307.
- Poulsen, H.F., 2004. Three-dimensional X-ray Diffraction Microscopy: Mapping Polycrystals and Their Dynamics. Springer, Berlin.
- Poulsen, H.F., Nielsen, S.F., Lauridsen, E.M., Schmidt, S., Suter, R.M., Lienert, U., Margulies, L., Lorentzen, T., Juul Jensen, D., 2001. Three-dimensional maps of grain boundaries and the stress state of individual grains in polycrystals and powders. *J. Appl. Crystallogr.* 34, 751–756.
- Proust, G., Tomé, C.N., Jain, A., Agnew, S.R., 2009. Modeling the effect of twinning and detwinning during strain-path changes of magnesium alloy AZ31. *Int. J. Plasticity* 25, 861–880.
- Quinta da Fonseca, J., Oliver, E.C., Bate, P.S., Withers, P.J., 2006. Evolution of intergranular stresses during in situ straining of IF steel with different grain sizes. *Mater. Sci. Eng. A* 437, 26–32.
- Salem, A.A., Kalidindi, S.R., Semiatin, S.L., 2005. Strain hardening due to deformation twinning in α -titanium: constitutive relations and crystal-plasticity modeling. *Acta Mater.* 53, 3495–3502.
- St-Pierre, L., Hériprié, E., Dextet, M., Crépin, J., Bertolino, G., Bilger, N., 2008. 3D simulations of microstructure and comparison with experimental microstructure coming from O.I.M analysis. *Int. J. Plasticity* 24, 1516–1532.
- Staroselsky, A., Anand, L., 2003. A constitutive model for hcp materials deforming by slip and twinning: application to magnesium alloy AZ31B. *Int. J. Plasticity* 19, 1843–1864.
- Timár, G., da Fonseca, J., 2014. Modeling twin clustering and strain localization in hexagonal close-packed metals. *Metall. Mat. Trans. A* 45, 5883–5890.
- Tome, C., Canova, G.R., Kocks, U.F., Christodoulou, N., Jonas, J.J., 1984. The relation between macroscopic and microscopic strain hardening in F.C.C. polycrystals. *Acta Metall.* 32, 1637–1653.
- Tomé, C.N., Lebensohn, R.A., Kocks, U.F., 1991. A model for texture development dominated by deformation twinning: application to zirconium alloys. *Acta Metallurgica Materialia* 39, 2667–2680.
- Troost, K.Z., van der Sluis, P., Gravesteijn, D.J., 1993. Microscale elastic-strain determination by backscatter Kikuchi diffraction in the scanning electron microscope. *Appl. Phys. Lett.* 62, 1110–1112.
- Wang, H., Wu, P.D., Wang, J., Tomé, C.N., 2013. A crystal plasticity model for hexagonal close packed (HCP) crystals including twinning and de-twinning mechanisms. *Int. J. Plasticity* 49, 36–52.
- Wilkinson, A.J., 1996. Measurement of elastic strains and small lattice rotations using electron back scatter diffraction. *Ultramicroscopy* 62, 237–247.
- Wilkinson, A.J., Meaden, G., Dingley, D.J., 2006. High-resolution elastic strain measurement from electron backscatter diffraction patterns: new levels of sensitivity. *Ultramicroscopy* 106, 307–313.
- Wilkinson, A.J., Tarleton, E., Vilalta-Clemente, A., Jiang, J., Britton, T.B., Collins, D.M., 2014. Measurement of probability distributions for internal stresses in dislocated crystals. *Appl. Phys. Lett.* 105, 181907.
- Wu, L., Agnew, S.R., Brown, D.W., Stoica, G.M., Clausen, B., Jain, A., Fielden, D.E., Liaw, P.K., 2008. Internal stress relaxation and load redistribution during the twinning–detwinning-dominated cyclic deformation of a wrought magnesium alloy, ZK60A. *Acta Mater.* 56, 3699–3707.
- Xu, F., Holt, R.A., Daymond, M.R., 2009. Modeling texture evolution during uni-axial deformation of Zircaloy-2. *J. Nucl. Mater.* 394, 9–19.
- Xu, F., Holt, R.A., Daymond, M.R., Rogge, R.B., Oliver, E.C., 2008a. Development of internal strains in textured Zircaloy-2 during uni-axial deformation. *Mater. Sci. Eng. A* 488, 172–185.
- Xu, F., Holt, R.A., Daymond, M.R., Rogge, R.B., Oliver, E.C., 2008b. Development of internal strains in textured Zircaloy-2 during uni-axial deformation. *Mater. Sci. Eng. A* 488, 172–185.
- Zambaldi, C., Zehnder, C., Raabe, D., 2015. Orientation dependent deformation by slip and twinning in magnesium during single crystal indentation. *Acta Mater.* 91, 267–288.
- Zeghadi, A., Forest, S., Gourgues, A.F., Bouaziz, O., 2007a. Ensemble averaging stress–strain fields in polycrystalline aggregates with a constrained surface microstructure – part 2: crystal plasticity. *Philos. Mag.* 87, 1425–1446.
- Zeghadi, A., N'Guyen, F., Forest, S., Gourgues, A.F., Bouaziz, O., 2007b. Ensemble averaging stress–strain fields in polycrystalline aggregates with a constrained surface microstructure – part 1: anisotropic elastic behaviour. *Philos. Mag.* 87, 1401–1424.
- Zhang, C., Li, H., Eisenlohr, P., Liu, W., Boehlert, C.J., Crimp, M.A., Bieler, T.R., 2015. Effect of realistic 3D microstructure in crystal plasticity finite element analysis of polycrystalline Ti–5Al–2.5Sn. *Int. J. Plasticity* 69, 21–35.
- Zhang, R.Y., Daymond, M.R., Holt, R.A., 2008. A finite element model of deformation twinning in zirconium. *Mater. Sci. Eng. A* 473, 139–146.
- Zhang, T., Collins, D.M., Dunne, F.P.E., Shollock, B.A., 2014. Crystal plasticity and high-resolution electron backscatter diffraction analysis of full-field polycrystal Ni superalloy strains and rotations under thermal loading. *Acta Mater.* 80, 25–38.
- Zhao, Z., Ramesh, M., Raabe, D., Cuitino, A.M., Radovitzky, R., 2008. Investigation of three-dimensional aspects of grain-scale plastic surface deformation of an aluminum oligocrystal. *Int. J. Plasticity* 24, 2278–2297.